scientific reports

Check for updates

OPEN

Application of concentrated solar energy in postprocessing of selective laser melted Ti6Al4V alloy through simultaneously gas nitriding and heat treatment

Lucia-Antoneta Chicos[1]✉, Jose Rodríguez[2], Inmaculada Cañadas[2], Jose Galindo[2], Grzegorz Cempura[3], Adam Kruk[3], Maciej Ziętara[3], Adam Gruszczyński[3], Mihai Alin Pop[4], Sebastian Marian Zaharia[1] & Camil Lancea[1]

Additive manufacturing is revolutionizing sustainable manufacturing by optimizing production processes and enhancing material and energy efficiency, reducing waste, and lowering resource consumption. Its integration with renewable energy sources further amplifies these benefits by reducing time, energy consumption and minimizing ecological impact. Currently, no studies have reported on high-temperature gas nitriding or the combined thermochemical and thermal treatment of Ti6Al4V alloy produced by selective laser melting (SLM) in a solar furnace (SF) using Concentrated Solar Energy (CSE) as a clean, renewable energy source. This paper presents the first study on the simultaneous thermal and gas nitriding thermochemical treatment of the Ti6Al4V ELI alloy manufactured by SLM, carried out in a SF using CSE and reducing post-processing times. Samples made of SLM Ti6Al4V ELI alloy were subjected to gas nitriding in the SF at temperatures of 900, 1050, and 1200 °C with short holding times of 5, 10, and 15 min. SEM–EDS, XRD analyses, and micro-Vickers hardness tests conducted on samples nitrided in SF, using CSE, confirmed the development of a nitrogen compound layer and a nitrogen diffusion zone, accompanied by a significant increase in microhardness, but achieved within a considerably shorter processing time. Total post-processing time for gas nitriding in the SF is up to 73% shorter than in conventional furnace. Simultaneously with gas nitriding thermochemical treatment, as-fabricated microstructure of Ti6Al4V ELI alloy, an acicular α′ martensite, was transformed into α + β with different morphologies. This paper demonstrates the integration of high-temperatures solar energy technology into the thermal post-processing of Ti6Al4V alloy, manufactured by the SLM additive manufacturing process, through nitriding thermochemical treatments.

Keywords Concentrated solar energy, Additive manufacturing, Ti6Al4V, Selective laser melting, Nitriding, Post-processing

Abbreviations

AM	Additive manufacturing
BCC	Body centred cubic
CSE	Concentrated solar energy
EDS	Energy dispersive X-ray spectroscopy
EE	Electric energy
EF	Electric furnace
ELI	Extra low interstitial

[1]Department of Manufacturing Engineering, Transilvania University of Brasov, 5 Mihai Viteazu, 500174 Brasov, Romania. [2]CIEMAT - Plataforma Solar de Almería, Ctra. de Senes Km 4.5, P.O. box 22, 04200 Tabernas, Almería, Spain. [3]International Centre of Electron Microscopy for Materials Science, AGH University of Science and Technology, 30 Mickiewicza Ave, 30-059 Krakow, Poland. [4]Department of Materials Science, Transilvania University of Brasov, 1 Colina Universitatii, 500084 Brasov, Romania. ✉email: l.chicos@unitbv.ro

FC	Furnace cooling
FCC	Face-centered cubic
HCP	Hexagonal close-packed
LOM	Light optical microscopy
ODL	Oxygen diffusion zone
OM	Optical microscopy
PSA	Plataforma Solar de Almeria
SCADA	Supervisory control and data acquisition
SEM	Scanning electron microscopy
SF	Solar furnace
SLM	Selective laser melting
SLMed	Selective laser melted
XRD	X-ray diffraction

In recent years, both researchers and industries have shown considerable interest in AM technologies, particularly SLM, because they enable the rapid fabrication of complex, lightweight, and customized components with efficient material use[1,2]. Today, hard materials or materials with a high melting point can be produced with SLM, such as Ti6Al4V alloy. Additionally, the industry recognizes AM as a green technology to achieve green and sustainable manufacturing due to less raw material requirements, which produces less waste, reducing scrap and carbon footprint[3]. Aerospace, automotive, chemical industries, marine applications, various corrosive environments, sports equipment and medicine extensively use titanium and its alloys. In the medical field, titanium is often used to replace heart valves, joints, and bones. Ti6Al4V alloy stands out for its high strength, excellent toughness, low specific weight, good resistance to corrosion, outstanding biocompatibility, and relatively low elastic modulus[4,5]. However, its low elastic modulus and thermal conductivity make it challenging to manufacture complex components using conventional processing methods[4]. Additive manufacturing technologies, on the other hand, enable the production of such complex parts. Because of their poor tribological properties, such as low abrasive wear resistance[1,2], poor fretting behavior, and a high coefficient of friction[6,7], industries rarely use titanium and its alloys in mechanical applications involving moving components. In biomedical applications, long-term implants made from titanium, particularly in artificial joints, can release wear particles that may trigger osteolysis and lead to implant rejection. Accordingly, various methods have been proposed for enhancing the mechanical, tribological and biocompatibility performance of Ti alloys such as heat processing and surface thermochemical treatments[2,8].

The most well-known and used thermochemical treatments for titanium and its alloys are nitriding[6,9], oxidation[2,4] and carburizing[8,10] which allow improving the surface properties. Nitriding has proven to be beneficial for titanium and its alloys because it allows obtaining a high hardness due to the surface compounds TiN and Ti_2N and also the substantial solubility of nitrogen in the α-phase. In this way, there is a gradual transition from the surface layer with high hardness to the softer substrate (bulk material)[2]. Different methods are used for the deposition of TiN layers on titanium substrate and its alloys, such as laser nitriding[10,11], plasma nitriding[8,12], ion implantation[8,13] or gas nitriding[5,7]. Gas nitriding stands out as a simple and cheap method because it does not require special equipment[8,9] and also is independent of the geometry of the sample which is a major advantage of this method. It is also well known that gas nitriding reduces the fatigue limit of titanium alloys, nitrided layers exhibit high hardness, which enables them to withstand high temperatures, and high wear and corrosion resistance[1,14]. A disadvantage of gas nitriding of titanium alloys is carried out at high temperatures (650–1000 °C) and longtime of up to 100 hours[8,10] either under the atmospheric pressure or in rarefied nitrogen. Prolonged exposure to high temperatures causes irreversible grain growth in the titanium matrix, resulting in brittle surface layers and a significant decrease in the mechanical properties of nitrided workpieces[1,13]. It is also well known that titanium is inherently highly reactive and has a strong chemical affinity for oxygen, which intensifies at temperatures above 600 °C. Therefore, treatments must be carried out in controlled atmosphere[14,15]. An effective approach to eliminate the negative consequences of high temperatures nitriding is to decrease the nitriding time as well as to identify some factors that can lead to intensification of the process[6] which allow providing the effective surface strengthening. The use of vacuum technology elements and corresponding initial deformation texture can allow intensifying the process of nitriding of titanium alloys in molecular nitrogen but the time of treatment remains still long.

SLM is an AM process through which components are built by selectively melting powder layers, with a focused laser beam, from various engineering metallic materials[16,17]. Regarding Ti6Al4V due to the specific process conditions, after SLM the as-fabricated microstructure of Ti6Al4V consists of a fine acicular martensite (α′ phase)[18]. This acicular martensitic microstructure is unstable, with internal stress, and oriented. Studies have shown that Ti6Al4V alloy components fabricated through SLM have high yield strength, high ultimate tensile strength than those fabricated using traditional casting processes but a low ductility and low corrosion resistance as the result of the large quantity of α′ phase[1,18]. Therefore, the microstructure of the as-fabricated parts could only be modified by using post-processing heat treatment to improve mechanical properties[8,18] both for Ti6Al4V and other alloys [16,17,19,20]. Gas nitriding effectively enhances the tribological and mechanical properties of SLM Ti6Al4V parts, which often have complex geometries such as medical implants, because the method operates independently of samples/parts shape[1,8] despite its long treatment duration[14]. The high-temperature gas nitriding process might be beneficial for the microstructure of Ti6Al4V produced by SLM process (which is an acicular martensite, α′ phase) because this microstructure must be subjected to heat treatment to improve its mechanical properties. The temperature, holding time, and environment, used in the gas nitriding process, lead to transformation of initial acicular martensite into microstructure consisting of α + β phase. Therefore, it can be considered as simultaneous thermal and thermochemical treatment of Ti6Al4V produced by SLM process. This

will allow a considerably shortening the post-processing time of Ti6Al4V parts manufactured by SLM. To date, there are very few studies on SLM Ti6Al4V gas nitriding and the existing ones are carried out in conventional (electric) furnaces. Studies have also been reported on the in-situ nitriding of Ti6Al4V by mixing different concentrations of nitrogen with Ar[21,22] as well as studies on subjecting, first, commercially pure titanium (CP–Ti) powder to a heat treatment in N_2 environment and then processed by AM[23,24]. To reduce nitriding time, preliminary studies demonstrated a great reduction in the nitriding time when the process is carried out in solar furnaces due to the activating effect of concentrated solar energy on thermochemical processes at high temperature[14,15]. In[25,26] was reported the use of CSE can be applied as an alternative to other types of energy beams for treating and modifying the surfaces of metallic materials. By delivering intense energy to small areas, CSE rapidly achieves high temperatures in very short times that accelerate diffusion processes. Rodriguez et al.[14] used concentrated solar energy in gaseous nitriding of Ti6Al4V alloy discs as a renewable energy and alternative to conventional processes. The treatment was carried out in a Fresnel lenses solar installation at 1100, 1150 and 1200 °C with holding time of 10 min. They also studied the effect of treatment duration at 1200 °C for 5, 10, and 15 min, finding that the highest hardness (2100 HV) was achieved after 15 min, compared to 8 h required in an electric furnace. Other researchers[27,28] nitrided titanium alloys using CSE and Fresnel lenses[29], obtaining TiN and $TiN_{0.3}$ films approximately 6 µm thick in only 2 min. Rodríguez et al.[15] obtained films of TiN of 10 µm and 1400 HV after 15 min at 1000 °C while after 5 min, at the same temperature, TiN was already detected. It was observed improvements in time for the nitriding process[14] and the rate of deposition was faster than in conventional furnaces[27,28].

To date, researchers have not published any studies on high-temperature gas nitriding or on the simultaneous thermochemical and thermal treatment of Ti6Al4V alloy produced by the SLM process in a solar furnace using CSE as a renewable energy source. Therefore, a first objective of the paper is the high-temperature gas nitriding of Ti6Al4V produced by SLM process in solar furnace using CSE, as an alternative to conventional post-processing that employ electrical furnaces. In the paper, attention was also paid to the effect of concentrated solar radiation on the activation of the gas nitriding process of Ti6Al4V produced by SLM technology when solar furnace is used, which will result in reducing the thermochemical treatment time.

Materials and methods

Material and manufacturing process

Cubic samples measuring 10 × 10 × 10 mm were fabricated by selective laser melting using a Sisma Mysint100 RM machine, from Ti6Al4V ELI powder in an Argon atmosphere. The composition of the Ti6Al4V ELI alloy powder, supplied by Carpenter Additive, is detailed in Table 1. All samples were manufactured in the same batch with the following process parameters: laser power of 200 W, layer thickness of 25 µm, hatch space of 100 µm, scanning speed between 1000 and 1500 mm/s. The building axes of samples were parallel to the Z direction and on the core surfaces it was used the *island* scanning strategy. In order to preserve the microstructure as it resulted after the selective laser melting, the samples were not subjected to stress relief treatment.

Gas nitriding thermochemical treatments

The gas nitriding thermochemical treatments were carried out in the horizontal solar furnace, SF40, from the research center Plataforma Solar de Almeria (PSA), Spain. Solar furnace, SF40, can deliver up to 40 kW power at peak concentration ratios exceeding 7000 kW/m^2 (7000 suns)[30]. All thermochemical treatments were carried out in a mixed gas atmosphere composed of N_2—5% H_2 with heating and cooling rate of 80 °C/min and an Ar flow of 400 l/h. Inside the spherical vacuum chamber (Fig. 1a), the samples were placed on a zirconia felt plate and for measuring and monitoring the temperature of the thermochemical treatment, type K thermocouples were used. The internal temperature of each sample was monitored by inserting a K-type thermocouple (TK01) into a hole, 8 mm deep, situated at the base of the sample. The SCADA (supervisory control and data acquisition) software system was used to control and monitor radiation, temperature, shutter aperture, test table movement, as well as data acquisition.

To remove impurities and oxygen from the spherical vacuum chamber, it was cleaned with one flow of Ar and two of N_2, before each gas nitriding treatment. Gas nitriding was performed at different temperatures, below and above β-transus (995 °C), presented in Table 2. For comparative analyses, gas nitriding treatments in the electric furnace (EF) were also carried out. Gas nitriding was performed in Nabertherm electric furnace, in N_2 gas at atmospheric pressure and heating and cooling rate of 20 °C/min (maximum heating rate allowed by the Nabertherm furnace). Temperatures and holding times are also presented in Table 2. The nitriding thermochemical treatment cycle (900 °C, 15 min) for sample S11 (in EF, using conventional energy) and S21 (in SF, using CSE) in Fig. 1b and c is presented. The key stages underlying the entire experimental procedure are illustrated in the simplified diagram shown in Fig. 1d.

Characterization methods

Cross-sections of both the as-fabricated SLM Ti6Al4V samples and those subjected to gas nitriding thermochemical treatment were embedded in resin and prepared through grinding and polishing using a LaboPol-Struers machine. Subsequent chemical etching was performed with Kroll's reagent (100 mL distilled

Powder	Titanium [%]	Aluminium [%]	Vanadium [%]	Iron [%]	Oxygen [%]	Carbon [%]	Nitrogen [%]	Hydrogen [%]	Yttirum [%]	Other [%]
Ti6Al4V ELI	balance	5.50–6.50	3.50–4.50	0.25	0.13	0.08	0.03	0.0125	0.005	< 0.10

Table 1. Ti6Al4V ELI powder composition.

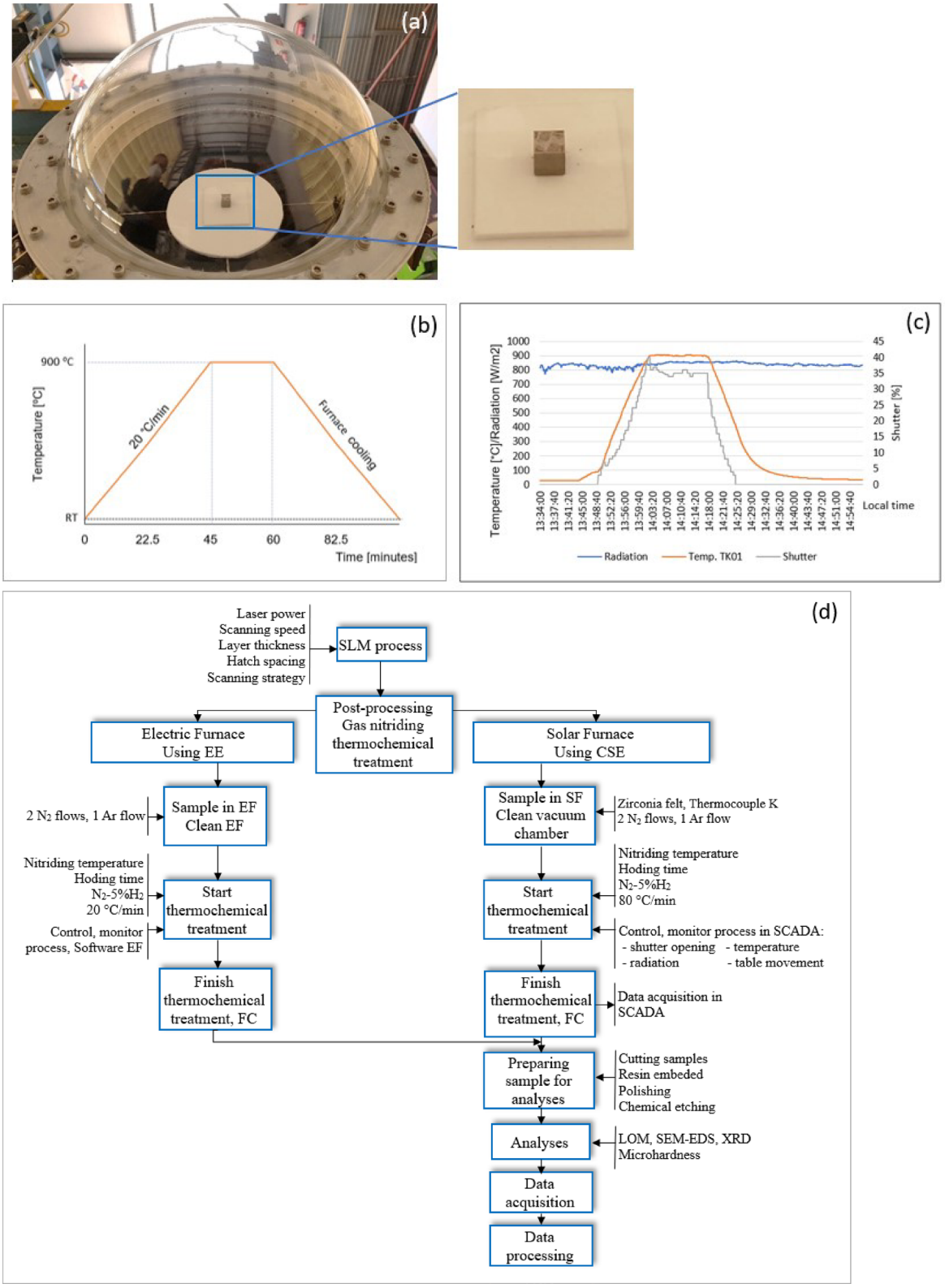

Fig. 1. Gas nitriding thermochemical treatment. (**a**) Sample inside vacuum chamber of SF40 before gas nitriding with CSE; (**b**) Thermal cycle of S11 sample (900 °C, 15 min) in EF; (**c**) Temperature, radiation, and shutter aperture during gas nitriding of S21 sample in SF (900 °C, 15 min); (**d**) simplified diagram of the overall experimental procedure.

Sample number	Furnace	Temperature [°C]		Holding time [minutes]	Cooling
		Below β-transus	Above β-transus		
S10	Solar furnace	900		5	Furnace cooling
S4		900		10	
S11		900		15	
S12			1050	5	
S5			1050	10	
S13			1050	15	
S14			1200	5	
S7			1200	10	
S15			1200	15	
S19	Electric furnace	900		5	
S20		900		10	
S21		900		15	
S16			1050	5	
S17			1050	10	
S18			1050	15	
S23			1200	5	
S22			1200	10	
S24			1200	15	

Table 2. Gas nitriding thermochemical treatments.

H_2O, 6 mL HNO_3, 3 mL HF) for five seconds, followed by rinsing with water and ethanol. Optical microscopy (OM) was carried out on LEICA DR IRM and ZEISS Axio Imager microscopes. Scanning electron microscope (SEM), Merlin Gemini II of ZEISS, was used for SEM analysis which is equipped with an electron dispersive spectrometer (EDS, Bruker Quantax 800). Energy dispersive X-ray spectrometry (EDS) mapping was used to evaluate structural characteristics down to an atomic level. The composition of the nitrided surfaces was determined by X-ray diffraction (XRD) analyses carried out with D8 Advance Brucker diffractometer using Cu K-α radiation and a 2θ range of 20–90°. Vickers microhardness was measured on the cross-sections of the samples with FM 700 microhardness tester under a constant load of 100 gf, for 10 s. 5 measurements were made, in the horizontal direction, onto the nitrogen compound layer (where it is clearly visible) and on the zone/layer in the upper part of the cross-section (where the compound layer should have been). The average value of the five measurements was used in the graphic representation of the microhardness evolution. Another 5 measurements were made from the surface to the inside of the sample, starting from the third indentation among the five made in the horizontal direction. To measure the thickness of the nitrogen compound layers, SEM and OM micrographs were analyzed using Fiji[31] and ZEISS ZEN software.

Results and discussion

It is well known that the microstructure of SLM material is obtained by extremely high cooling rate, inherent in the SLM process[18,32] and it is completely different from that of Ti6Al4V obtained by classical technologies (casting or forged)[33,34]. Consequently, we could expect a different process kinetics of the nitriding process, as well as different morphologies and properties of the microstructures. In this research, as expected, the as-fabricated SLM Ti6Al4V microstructure contains both metastable acicular martensite (α′ phase) and elongated prior β grains (Fig. 2a,b). Temperature and fast-growing rate result in α′ needles with specific orientation[32,33] within prior β grain.

After the nitriding thermochemical treatment in the solar furnace, the samples changed their color from bright gray (the color of the Ti6Al4V alloy obtained by SLM) to light or dark golden, depending on the temperature and holding time. The change of the sample color to golden signifies the formation of a nitrogen diffusion zone and, correspondingly, the development of a nitrogen compound layer, findings that align with those reported in previous studies[2,14]. The surface appearance of the samples subjected to nitriding thermochemical treatment in the electric furnace (EF) differed notably from those treated in the solar furnace (SF). Following EF nitriding, most samples exhibited a brown or dark gray surface layer, depending on the temperature and holding time. This gray layer was brittle, and its removal revealed the underlying final surface morphology of the EF nitrided samples.

SEM and XRD analyses revealed that, during the gas nitriding process in EF, the oxidation of the SLM Ti6Al4V samples also occurred. The resulting oxide layer impeded the nitriding process from proceeding properly, even though, before the actual nitriding, the electric furnace was cleaned by impurities and oxygen following the same preparatory steps applied in the SF process. Some authors[35] consider that argon gas impurities, including oxygen and water vapor, could be potential sources of contamination. The resulting oxide layer inhibits the nitrogen diffusion into the substrate material. This phenomenon has also been observed in previous published studies[36].

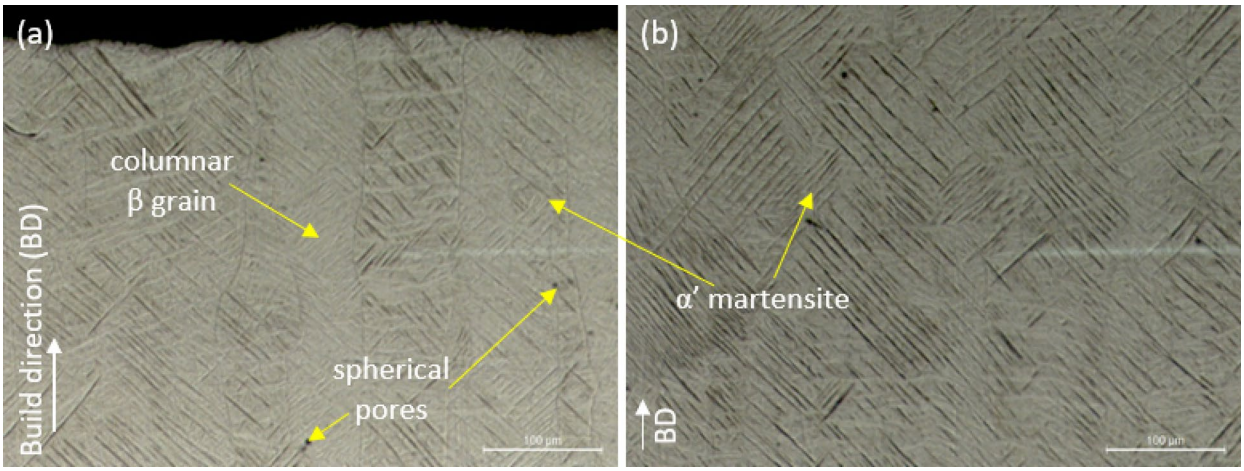

Fig. 2. Microstructure of as-fabricated SLM Ti6Al4V ELI. Optical micrographs of the top (**a**) and internal (**b**) area of sample cross-section.

Gas nitriding of SLM Ti6Al4V alloy below β-transus

The thermochemical nitriding treatment at 900 °C, with a holding time of 5 min, carried out both in SF using CSE (Fig. 3a) and in EF (Fig. 4a) did not result in the formation of a nitrogen compound layer on the surface of the samples, S10 and S19 respectively, very clearly visible and delimited, as illustrated in the OM and SEM micrographs in Figs. 3b,4b, and 3c, 4c, respectively. Microscopic images in Figs. 3b and 4b indicate that, following thermochemical treatment at 900 °C for 5 min, the microstructures of samples S10 and S19 remain predominantly composed of α′ martensite (because of low temperature and short time).

Also, the long, columnar prior β grains, specific to the SLM Ti6Al4V microstructure, are still visible both in the cross section of the S10 samples, nitrided in SF (Fig. 3b), and of the one treated in EF (Fig. 4b).

Line scan SEM–EDS analysis presenting the elemental distribution along the scanning path on the top surface of the cross-section is shown in Fig. 3c–e. On the upper surface of sample S10, a light-colored area in the outermost surface is observed, which can be attributed to a nitrogen diffusion zone within the Ti6Al4V substrate. Specifically, an interstitial solid solution of nitrogen in the HCP α-titanium phase, as previously reported[8,36]. Figure 3d and e illustrate that the nitrogen concentration in the outermost white area is higher than Al and V, indicating that a nitriding duration of only 5 min is sufficient to generate a nitrogen-rich surface layer. Aluminum and vanadium are expelled from N—rich area toward the interior of the sample. At the peak intensity within the white region, the nitrogen content (mass percent, wt%) reaches 11.197%, while aluminum and vanadium contents are 3.872% and 0.0%, respectively. Beneath this outermost white zone, nitrogen concentration gradually decreases with depth, towards the inside of the sample, whereas Al slightly increases. A very slightly increase in vanadium content is also observed within the β-phase laths. These results reveal that during SF gas nitriding, using CSE, additional factors such as solar radiation which contribute to the intensification of nitrogen diffusion into the SLM Ti6Al4V alloy[37]. The SEM micrograph in Fig. 3c reveals a predominantly bilamellar microstructure, characterized by α-phase laths embedded in a β-phase matrix (lamellae—like). Although the α lamellar phase dominates, the presence of β-phase lamellae are also discernible.

Following thermochemical gas nitriding in the electric furnace (EF) at 900 °C for 5 min, the surface of sample S19 became light brown (Fig. 4a), totally different from the appearance of sample S10 treated by SF gas nitriding. SEM (Fig. 4c) and EDS (Fig. 4d,e) analyses reveal the formation of a porous surface layer, attributed to oxidation occurring during gas nitriding in EF. This oxidation is also confirmed by the line scan SEM–EDS results (Fig. 4e), which demonstrate a substantial presence of oxygen. The formation of this oxide layer impeded nitrogen uptake, due to the greater affinity of titanium for oxygen than for nitrogen[38]. Oxygen has a higher solubility in α-phase, which makes it difficult to avoid the formation of oxides, as also noted in reference[2]. It should be mentioned that, regarding the thermochemical gas nitriding treatment, in the electric furnace, the oxidation appeared regardless of nitriding temperature and holding time, as will be discussed in the subsequent subsection. The optical microscopy (Fig. 4b) reveals, much more clearly than for the S10 sample nitrided in SF, the presence of α′ martensite and columnar prior β grains.

SEM analysis (Fig. 5a,b) carried out on internal areas of samples subjected to gas nitriding at 900 °C for 5 min reveals that, due to the short holding time, the initial microstructure characteristic of the Ti6Al4V alloy produced by SLM, primarily composed of α′ acicular martensite, was not entirely transformed into the lamellar α + β phase (the microstructure is a mixture of α and β plates)[18,33]. However, there are fine needles of the α′ phase in the microstructure. It is found that in sample S10 treated in SF (Fig. 5a), vanadium segregation and subsequent β-phase formation is more prominently compared to sample S19, which was nitrided in EF (Fig. 5b).

Figure 6a–e presents the results of thermochemical gas nitriding treatment conducted using CSE for 10 min. The LOM micrograph in Fig. 6b reveals that columnar grains can still be identified even though the holding time increased from 5 to 10 min. These initial columnar grains, were also identified in samples treated in EF, appear more distinctly defined in this case, with clearer grains boundary.

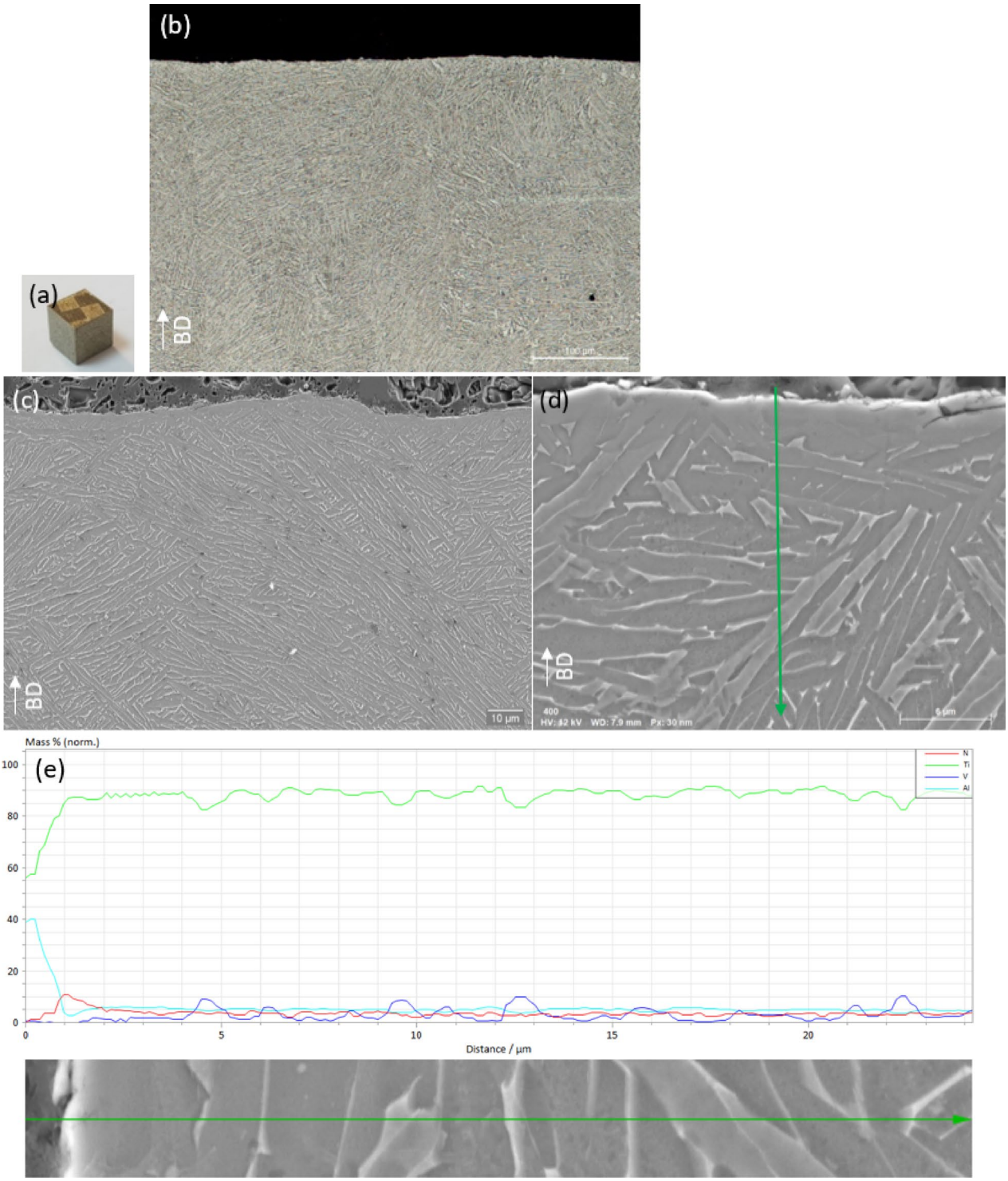

Fig. 3. Gas nitriding at 900 °C for 5 min in solar furnace. (**a**) sample S10 after nitriding, (**b**) cross-section microstructure from LOM on top part of the sample, (**c**) SEM image on the top part of S10 sample, (**d**,**e**) line scan SEM–EDS analysis on the top of S10 sample cross-section.

In the outermost region of the cross-section, intermittent white areas are identified in both the LOM (Fig. 6b) and SEM (Fig. 6c) micrographs, which are indicative of nitrogen-enriched areas. This high nitrogen concentration is corroborated by the line scan EDS analysis presented in Fig. 6d and e. As shown in Fig. 6e, the maximum nitrogen content, measured at a depth (point) of 1.206 µm, is 11.502%, while the concentrations of the alloying elements vanadium and aluminum are 0.931% and 3.057%, respectively. The underlying area beneath this nitrogen-rich surface layer also exhibits high nitrogen content relative to the sample interior, with nitrogen concentration gradually decreasing from the surface inward, consistent with expected diffusion behavior.

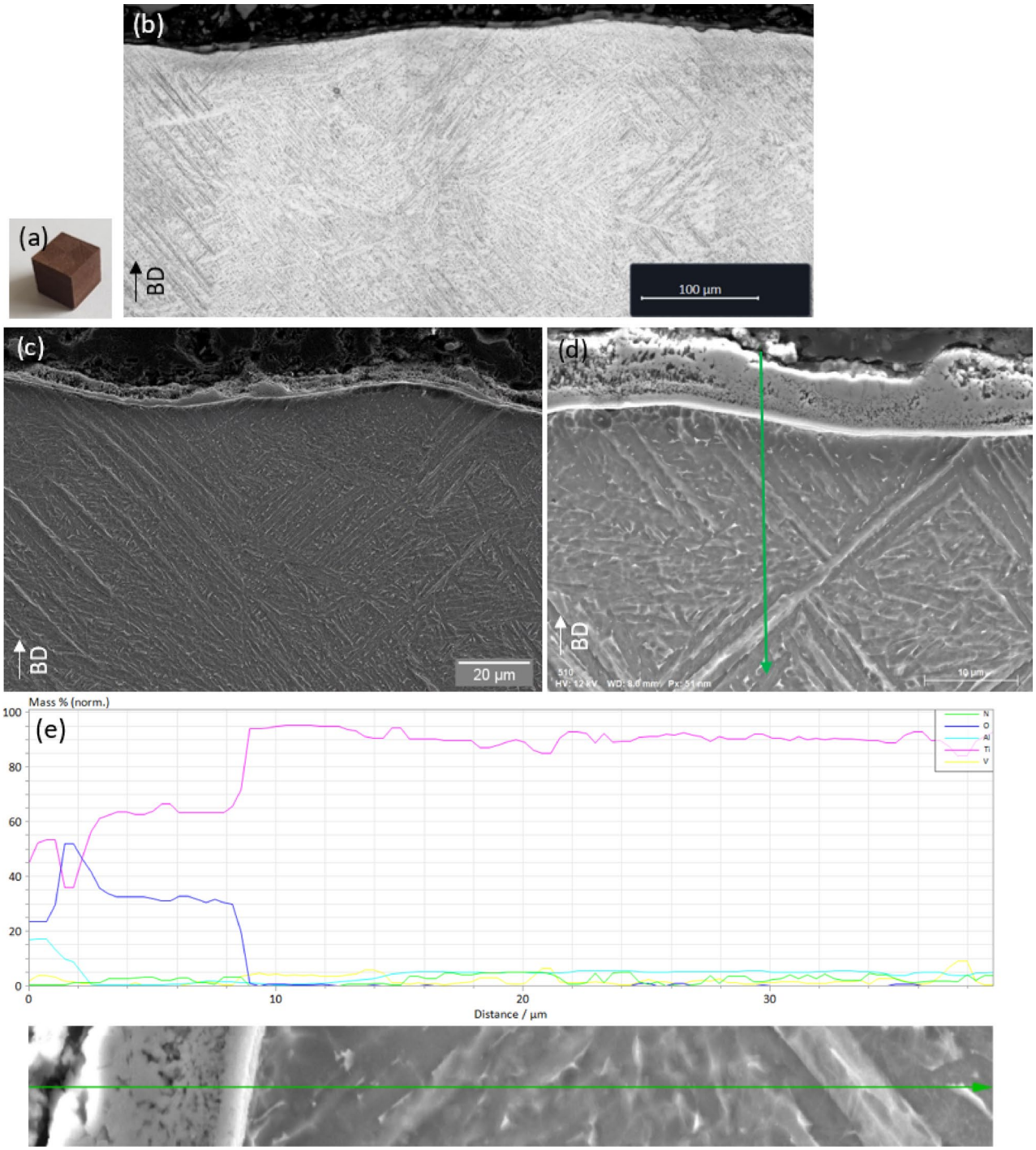

Fig. 4. Gas nitriding of S19 sample, at 900 °C for 5 min in electric furnace. (**a**) sample S19 after nitriding, (**b**) OM of cross-section microstructure on top part of the sample, (**c**) SEM image on the top part of S19 cross-section, (**d**,**e**) line scan SEM–EDS analysis on the top of S19 cross-section.

In the case of thermochemical gas nitriding conducted in EF at 900 °C for 10 min (Fig. 7a–e), SEM (Fig. 7c) and SEM–EDS (Fig. 7d–e) analyses reveal the formation of a porous surface layer on the sample surface. Beneath this, a continuous white layer is observed, as indicated in both Fig. 7c and d. SEM–EDS line scan analysis (Fig. 7e) confirms that these layers are characterized by a high O_2 concentration. Nitrogen content, by contrast, is extremely low, suggesting that oxidation was more intense than the nitriding. In the area labeled with 1 (Fig. 7e), located at a depth of 12.281 µm, the O_2 content reaches 28.022%, while N_2 is entirely absent (0.0%). In the subsequent layer (the area marked with 2), situated below the oxygen-rich region (label 1), nitrogen is extremely low with an average concentration of 0.45%, whereas O_2 has an average level of 0.92%.

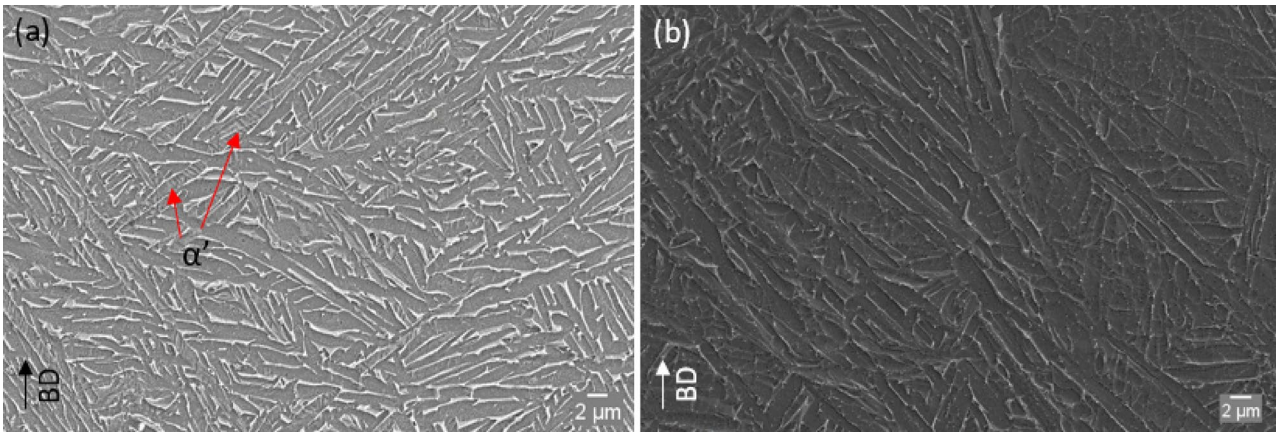

Fig. 5. Internal microstructure of SLM Ti6Al4V after nitriding at 900 °C, for 5 min. (**a**) microstructure of S10 sample nitrided in SF, (**b**) microstructure of S19 sample nitrided in EF.

The average concentrations of aluminum and vanadium are 2.23% and 2.96%, respectively. The absence or significantly low presence of nitrogen, in contrast to the sample nitrided in SF using CSE, is attributed to the absorption and deposition of surface oxides, which suppressed the nitriding process. It is well known that the oxidation process of Ti6Al4V is more intense than nitriding and the diffusion of nitrogen in titanium is slower than that of oxygen, as also reported in previous studies[35,37]. The thermochemical gas nitriding at 900 °C for 10 min also led to the transformation of acicular martensite α′ into a mixture of α-phase in matrix β, as observed in the interior microstructure of the samples (Fig. 8a,b). The microstructure of the S4 sample nitrided in SF (Fig. 8a) contains a higher volume fraction of α plates compared to S20 sample treated in EF (Fig. 8b) as well as sample nitrided in SF at the same temperature but with a holding time of 5 min (Fig. 5a).

Gas nitriding at 900 °C for 15 min, in SF, using CSE, resulted in higher absorption and diffusion of nitrogen in the SLM Ti6Al4V substrate (Fig. 9a–e) compared to nitriding in SF, for 5 and 10 min respectively, and nitriding in EF under identical thermochemical conditions (Fig. 10). The SEM (Fig. 9c) and SEM–EDS (Fig. 9d and e) analyses reveal the formation of a discontinuous white surface layer on sample S11, characterized by a high nitrogen concentration, which could be associated with the Ti_2N phase, as previously reported[8]. According to the SEM–EDS line scan (Fig. 9e), the nitrogen content reaches 13.36% at a depth of 1.32 µm. Beneath this layer, a continuous area (layer) is observed (Fig. 9c–e), containing an average nitrogen concentration of 3.86%. In this area, vanadium (an average of 1.56%) is expelled towards the interior of the substrate. In this layer, the β plate phase is absent present in minimal quantities. This area could correspond to the beginning of the nitrogen compound layer formation.

As observed in the samples nitrided in the EF at 900 °C for 5 and 10 min, the sample nitrided for 15 min (Fig. 10a–e) also exhibited the formation of a surface oxide layer, as confirmed by SEM and SEM–EDS analyses (Fig. 10c–e). The SEM–EDS line scan (Fig. 10e) indicates a high oxygen concentration within both the porous surface layer and the bright white layer, with a peak oxygen content of 33.38% detected at a depth of 11.58 µm. In contrast, the nitrogen content at the same location is significantly low, at only 2.29%. Unlike the SF nitrided sample (S11), the sample treated in EF (S21) does not exhibit the formation of a nitrogen compound layer, as evidenced in Fig. 10c–e.

Gas nitriding at 900 °C for 15 min resulted in transformation, to the greatest extent, of the α′ acicular martensite into a mixture of α and β- phases (Fig. 11a–c). In the microstructure of the sample nitrided in SF, primary columnar grains were no longer observed, but some areas still contain α′ acicular martensite. This indicates that the selected temperature and holding time were insufficient to fully transform the initial fine martensite into α and β phases (Figs. 11a,9b). It is also found that the α-phase laths appear slightly coarser compared to those observed following gas nitriding for 5 and 10 min at the same temperature.

Gas nitriding in EF at 900 °C for 15 min had a lower effect on the bulk microstructure of the SLM Ti6Al4V alloy, as seen in sample S21 (Fig. 11b,c) when compared to the microstructure of sample (S11) nitrided in SF. The microstructure of the sample S21 consists of a mixture of α and β and still contains columnar β grains (Fig. 11c) containing α′ acicular martensite, as also mentioned in the works[33,34]. It is found that the temperature of 900 °C, related to the thermochemical gas nitriding treatment, promotes coarsening of width of α and β- phase in the substrate material, particularly for nitriding in SF, as noted in earlier studies[39,40]. It is worth noting that most gas nitriding procedures reported in the literature employ significantly longer holding times, typically at least one hour[5,41], with only a few exceptions[14,27].

Gas nitriding of SLM Ti6Al4V alloy above β-transus

The samples made of SLM Ti6Al4V ELI alloy were subjected to the thermochemical gas nitriding treatment at temperatures, above β-transus, of 1050 °C and 1200 °C respectively with holding times of 5, 10, and 15 min, respectively. After the gas nitriding process, in SF, using CSE, all the samples exhibited a surface coloration from light to dark golden indicating nitrogen absorption and diffusion. In contrast, samples nitrided in EF obtained a color from light to dark gray indicating that an oxide layer was deposited on their surface (a brittle layer that

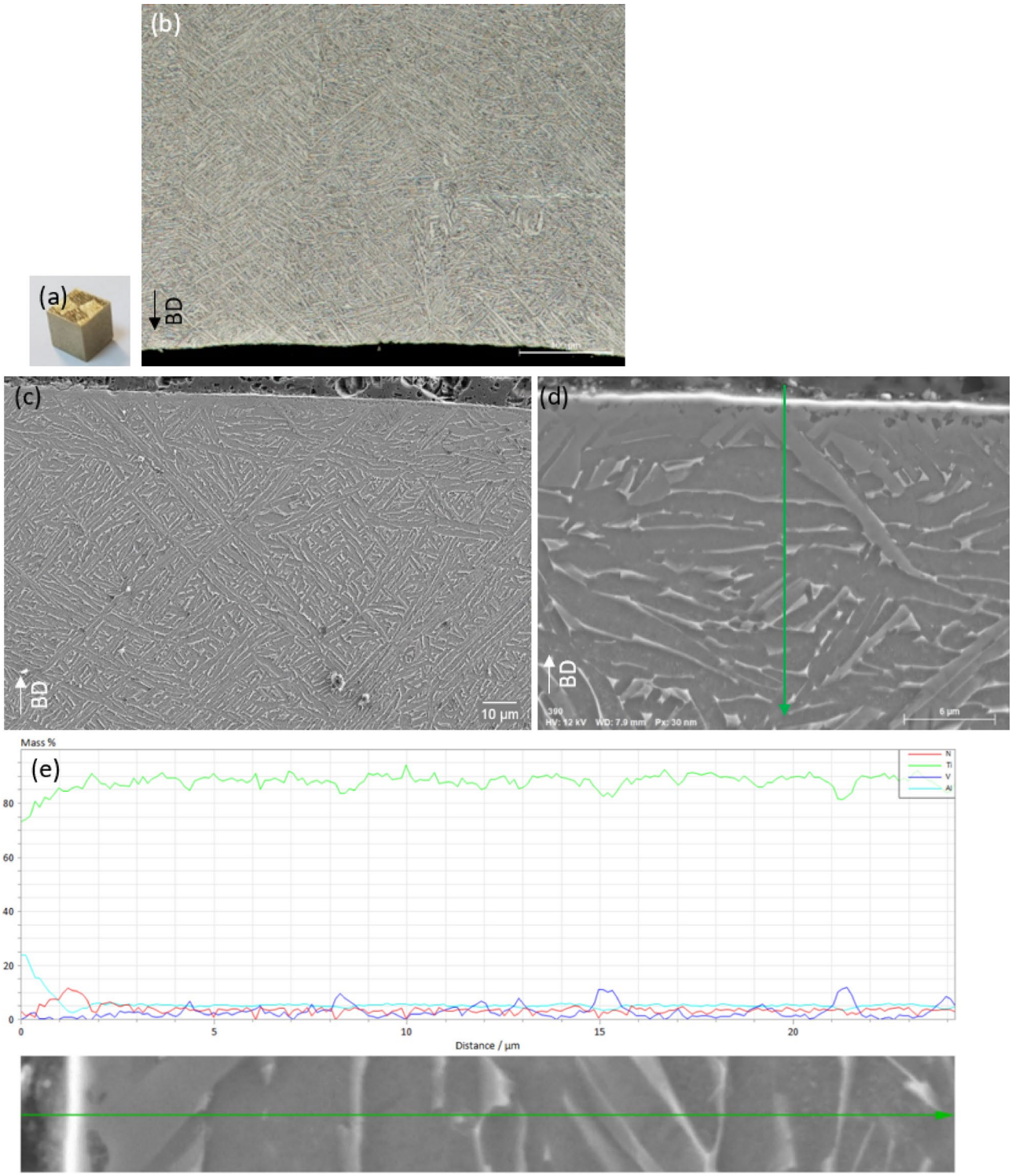

Fig. 6. Gas nitriding at 900 °C for 10 min in solar furnace. (**a**) sample S4 after nitriding, (**b**) cross-section microstructure from OM on top part of the sample, (**c**) SEM image on the top part of S4 sample, (**d**,**e**) line scan SEM–EDS analysis on the top of S4 sample cross-section.

was subsequently removed). Sample S12, nitrided in the SF at 1050 °C for 5 min, along with corresponding LOM and SEM–EDS analyses, is presented in Fig. 12a–e. The LOM and SEM micrographs (Fig. 12b and c) reveal the formation of a layer on the upper (labeled with A in Fig. 12c), lateral, and lower surfaces of the sample. This layer is clearly demarcated from the substrate by an irregular interface.

This area corresponds to the nitrogen compound layer (TiN + likely Ti_2N), while underneath the compound layer there is the nitrogen diffusion zone (α-Ti(N)). These interpretations align with findings reported in

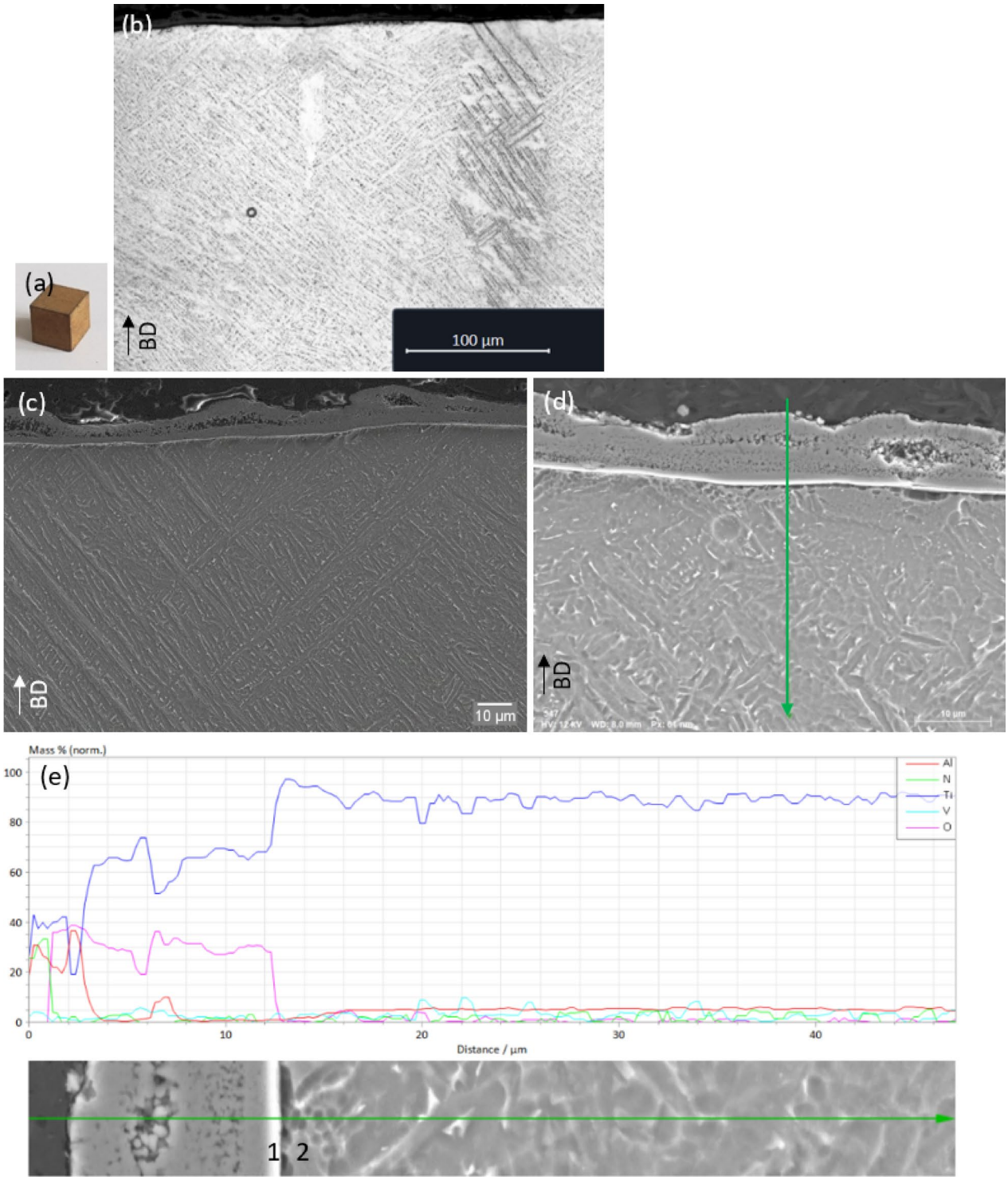

Fig. 7. Gas nitriding of S20 sample, at 900 °C for 10 min in electric furnace. (**a**) sample S20 after nitriding, (**b**) OM of cross-section microstructure on top part of the sample, (**c**) SEM image on the top part of S20 cross-section, (**d**,**e**) line scan SEM–EDS analysis on the top of S20 cross-section.

references[2,42] and are further supported by microhardness measurements. This compound layer was formed on all samples subjected to gas nitriding, in solar furnace, at temperatures above β-transus (1050 °C and 1200 °C respectively) and its thickness increases with increasing temperature and holding time. These findings are consistent with the papers[8,43]. The LOM (Fig. 12b) and SEM (Fig. 12c) micrographs of the cross-section of sample S12 clearly illustrate the formation of the nitrogen compound layer. Figure 12d and e show the result of the line scan SEM–EDS analysis in the upper part of the cross-section. It is found that the layer corresponding to the compound layer exhibits a high nitrogen concentration, containing an average percentage of 3.68%. The

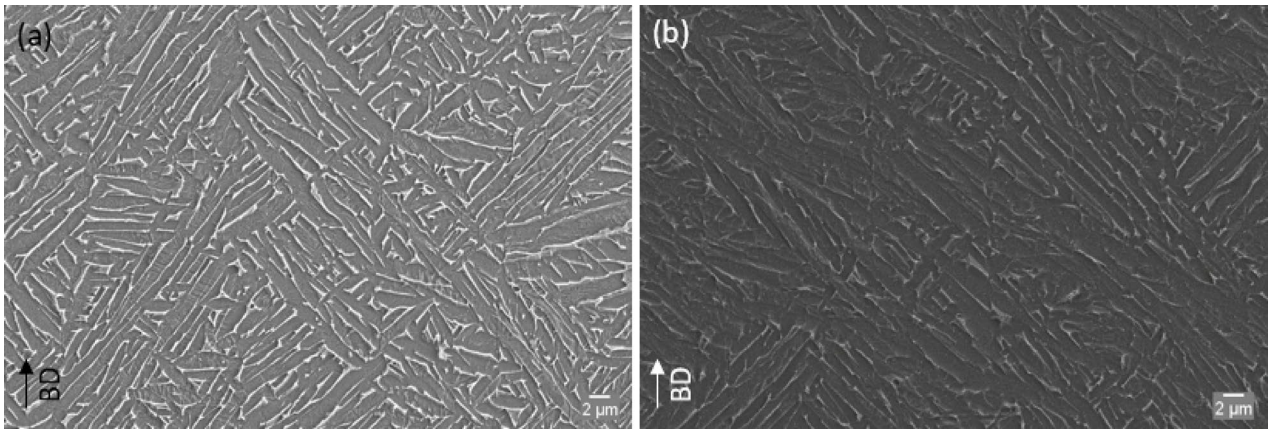

Fig. 8. Internal microstructure of SLM Ti6Al4V after nitriding at 900 °C, 10 min. (**a**) microstructure of S4 sample nitrided in SF, (**b**) microstructure of S20 sample nitrided in EF.

thickness of the nitrided layers, calculated as the average of six measurements, as well as the microhardness values, in Table 3 are summarized. Discussions on the microhardness results are addressed in the subsection 3.3.

The results of the analyses obtained after subjecting the sample S16 to gas nitriding in EF, at 1050 °C, for 5 min, in Fig. 13a–e are presented. In the LOM micrographs (Fig. 13b) and SEM (Fig. 13c), it is found the presence, in the upper part, of an area (labeled with B in Fig. 12c) completely different from the one obtained after nitriding in SF (Fig. 12b and c). Above this area, a layer is identified which, following the SEM–EDS line scan analysis (Fig. 13d and e), is confirmed to be an oxide layer because, in this layer, the average concentration of oxygen is 27.69%. Comparable areas to that labeled with B in Fig. 13c were also identified in the samples nitrided in EF at 1050 and 1200 °C, respectively, with holding times of 10 and 15 min. This area (layer) can be considered an oxygen diffusion zone (ODL) that led to a microstructure, in the largest proportion, bi-modal or duplex with α equiaxed grains. Since oxygen is an α stabilizer, its presence in a high percentage led to the formation of the area with the equiaxed microstructure[44,45], being the well-known greater affinity of titanium for oxygen than for nitrogen[45,46]. The higher volume fraction of α-phase in this area and the high temperature of thermochemical treatment determined the rapid formation of rutile (TiO_2)[44,47] according to the XRD analysis.

EDS analysis in the point 1 (Fig. 14a, spectrum 1) reveals that the chemical composition, listed in the inset (Fig. 14b), of this layer contains a high amount of oxygen, which confirms the result of the line scan analysis, that is, formation of oxides on the sample surface (likely, α case). Underneath this layer, the presence of some areas, separated from each other, that do not contain β-phase plates, was found (Fig. 14a, label C). The result of EDS analysis, in point 2 (Fig. 14c, spectrum 2) and line scan SEM–EDS (Fig. 13e) reveals that Al (percentage average of 4.05%, in line scan analysis) and N_2 (3.1%) have the highest percentages, which indicates that it is possible that these areas represent the nitrogen solid solution phase in Ti, α-Ti(N). It should be emphasized that the N-Kα, V-Lα, and Ti-Lα spectra overlap at approximately 0.39 keV[5,47]. Hence, the concentrations for nitrogen could be inaccurate.

Micrographs from the central area of the samples, after nitriding at 1050 °C, with a holding time of only 5 min, show a lamellar α + β microstructure (Fig. 15a–b). An increase in processing temperature promoted the increase of the α-phase lamellae, which is in accordance with[48,49]. In the microstructure of sample S12, nitrided in SF (Fig. 15a), it can be seen that the lamellae of α-phase are much more clearly delimited by β-phase, compared to the microstructure of S16 sample (Fig. 15b). Colonies of long parallel α plates appear in both microstructures (Figs. 12b,c, 13b,c) which is consistent with[50,51]. The microstructure of S12 sample contains more colonies, compared to that of S16 sample. In the latter, the presence of areas in which the lamellae of the α-phase are in the initial phase of formation and are not very well delimited by the β-phase (Fig. 15b) can be found. It is also found that the β-phase exhibits a lower vanadium content compared to the microstructure of S12 sample, nitrided in SF.

Increasing the holding time to 10 min during the thermochemical nitriding treatment in SF, at a temperature of 1050 °C, resulted in increased nitrogen absorption (Fig. 16a–e), also demonstrated by the dark golden color of the sample (S5) (Fig. 16a). The LOM and SEM micrographs of the cross-section of S5 sample (Fig. 16b and c respectively) reveal the presence of a nitrogen compound layer with a slightly greater thickness (an average value of 11.96 ± 2.85 µm) than the one after nitriding in SF, for 5 min (Fig. 12b,c, Table 3). Which proves that the holding time influences the thickness of the compound layer. Line scan SEM–EDS, shown in Fig. 16d–e, indicates the presence of nitrogen in the corresponding TiN layer (an average percentage of 3.83%). At the level of the microstructure (Fig. 16c and d), it is found that the area underneath the nitrided layer contains both the lamellar α + β and α equiaxed phase (duplex microstructure on narrow areas). As it was shown in other studies[5,7], nitrogen penetration into the substrate material, as an α stabilizer[38], leads to the formation of a microstructure with α equiaxed grains[52,53].

The results of the thermochemical nitriding treatment in EF are shown in Fig. 17a–e. The micrographs in Fig. 17b and c reveal the presence of the area (layer) with the bi-modal microstructure but the α-phase grains coarsened due to the longer holding time and the oxygen influence. Comparing with the sample nitrided in SF

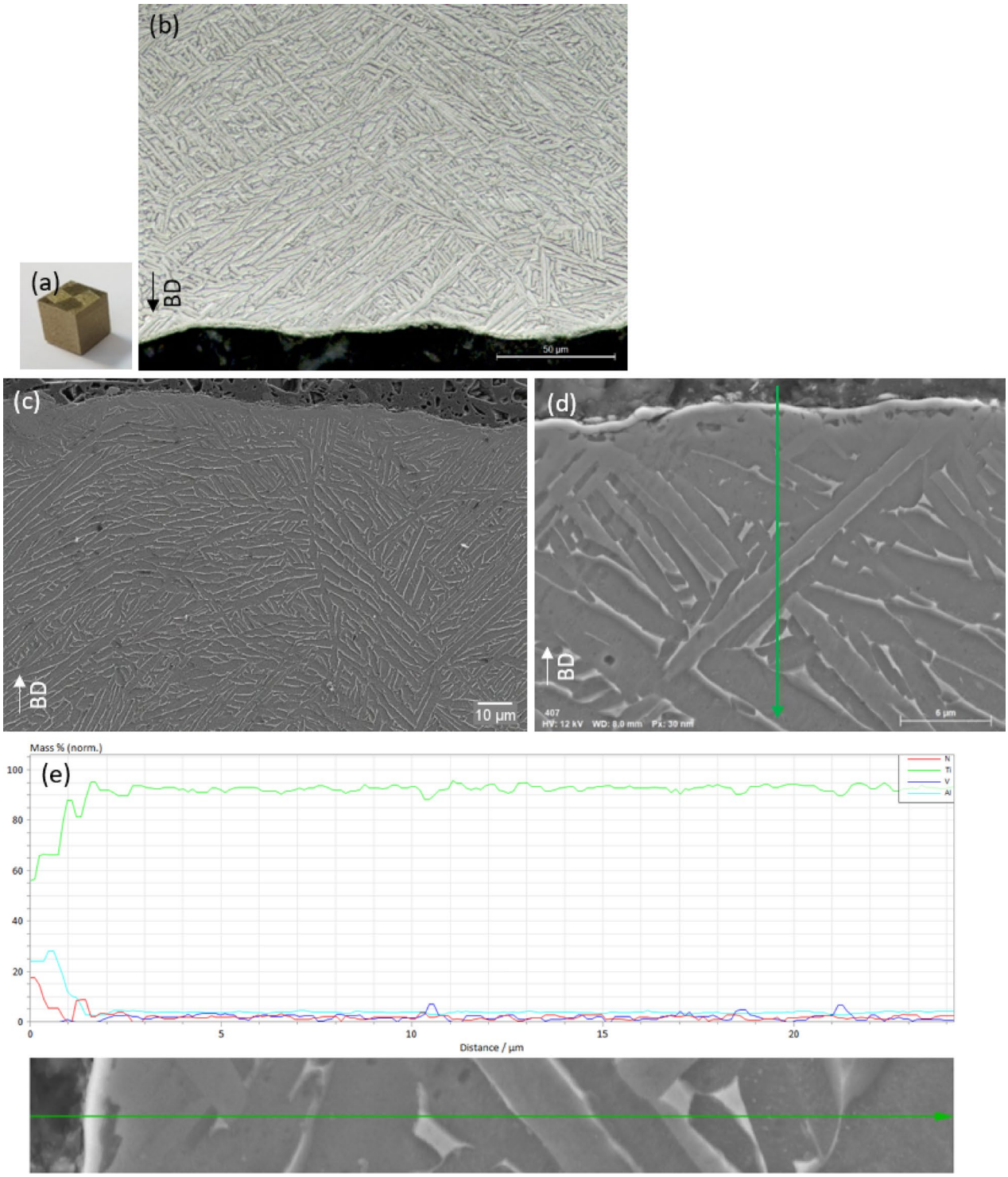

Fig. 9. Gas nitriding at 900 °C for 15 min in solar furnace. (**a**) sample S11 after nitriding, (**b**) cross-section microstructure from OM on top part of the sample, (**c**) SEM image on the top part of S11 sample, (**d**,**e**) line scan SEM–EDS analysis on the top of S11 sample cross-section.

(S5), no nitrogen compound layer is identified (Table 3), but the presence of the oxide layer is found (Fig. 17c–e). SEM–EDS line scan analysis (Fig. 17d–e), indicates a low concentration of nitrogen in the upper layers of the sample cross-section, also confirmed by the low microhardness compared to that after nitriding at 900 °C for the same holding time.

The gas nitriding thermochemical treatment at 1050 °C, for 10 min, determined, in the internal microstructure of the samples, the transformation of the α′ initial martensite into the Widmanstätten microstructure (Fig. 18a–d), a result that is in agreement with[2,14].

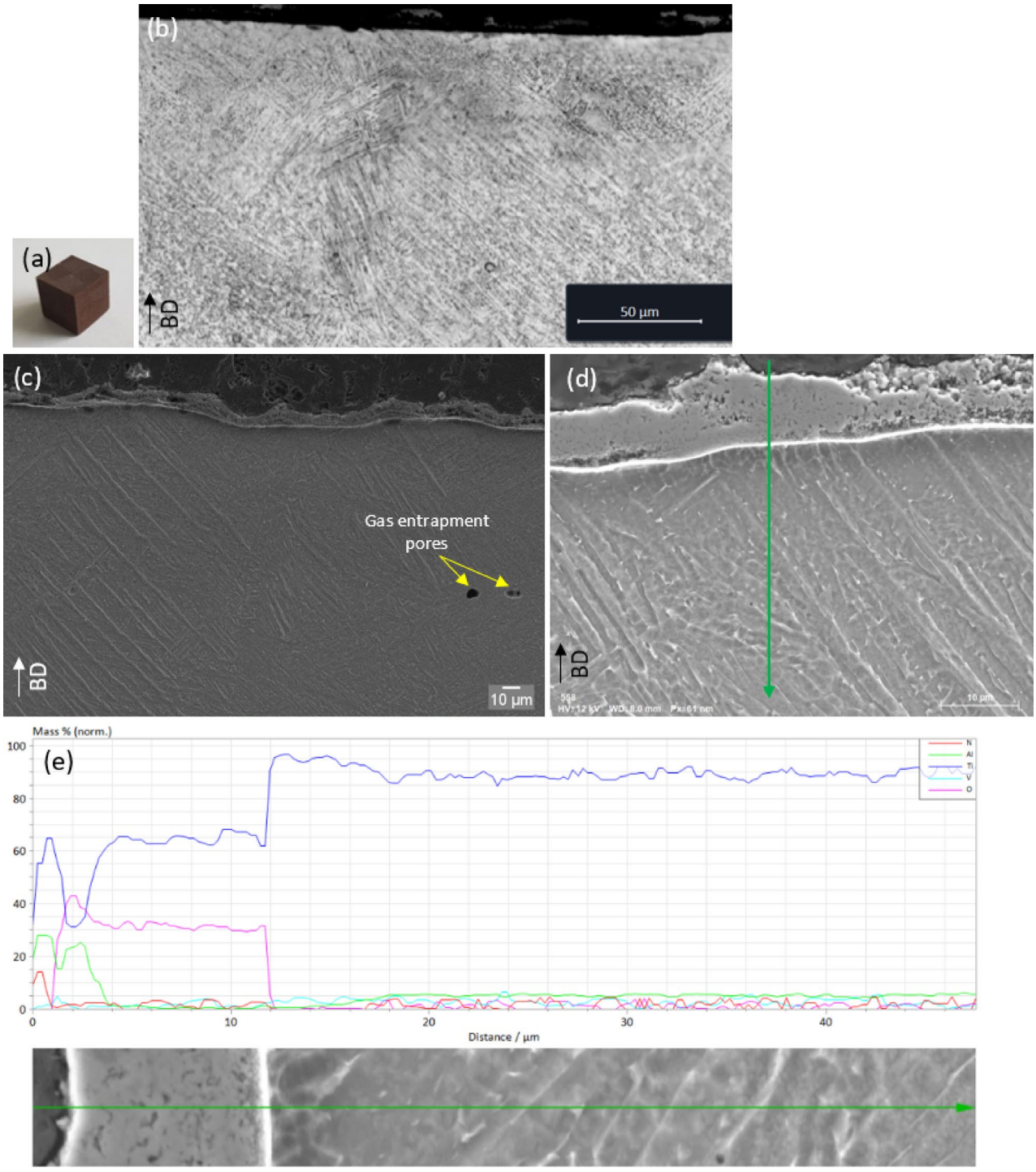

Fig. 10. Gas nitriding of S21 sample, at 900 °C for 15 min in electric furnace. (**a**) sample S21 after nitriding, (**b**) OM of cross-section microstructure on top part of the sample, (**c**) SEM image on the top part of S21 cross-section, (**d**,**e**) line scan SEM–EDS analysis on the top of S21 cross-section.

After gas nitriding at 1050 °C, for 15 min, in SF (Fig. 19a–e), the color of the sample surface became darker (dark gold), which proves that the deposited film is richer in nitrogen (Fig. 19a). LOM and SEM analyses of the cross-section of S13 sample (Fig. 19b,c), reveal an increase in consistency and thickness of the nitrided compound layer (Table 3). Additionally, a very thin, discontinuous, bright white layer is observed at the outermost surface of this compound layer (Fig. 19c–e). XRD analysis confirms the presence of the TiN phase within the compound layer. The average nitrogen content in this layer is 4.7%, nearly twice the value measured in the discontinuous areas (2.4% N_2) of the sample nitrided in EF at the same temperature and holding time (Fig. 20c–e).

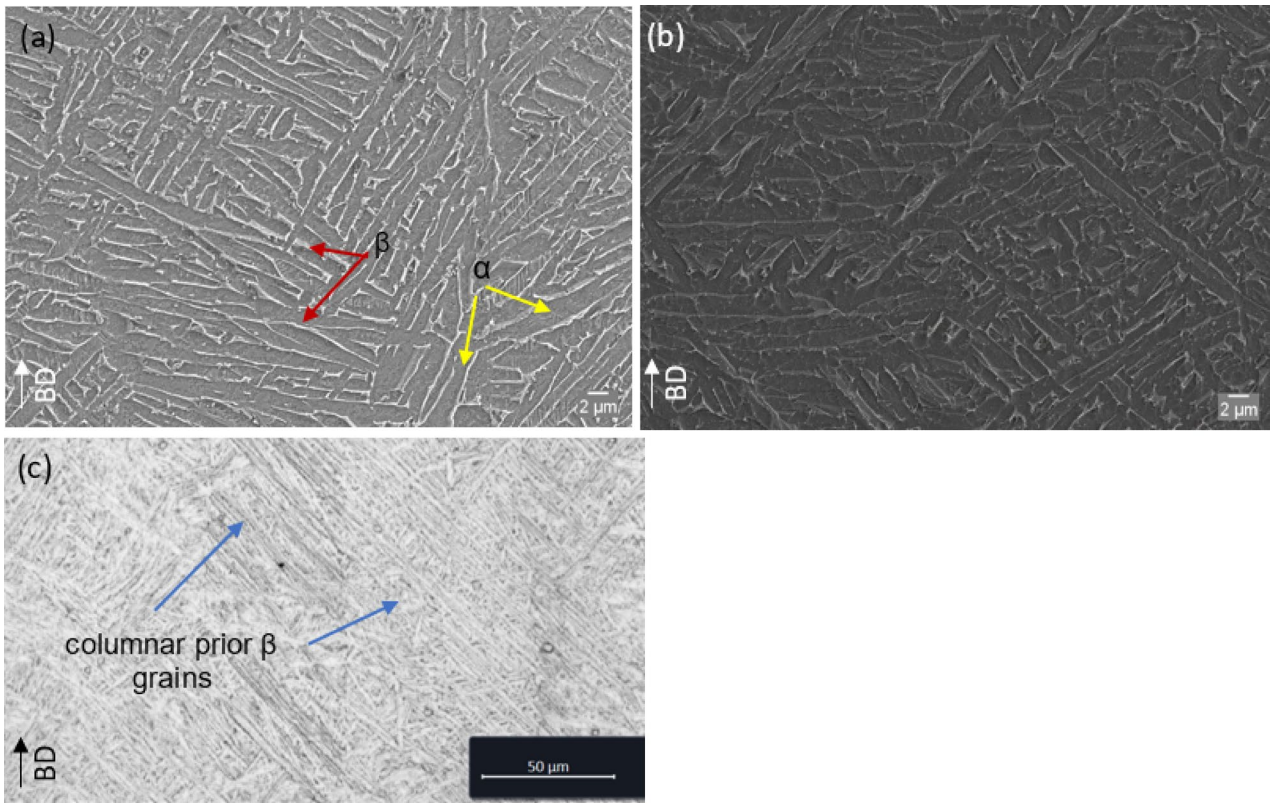

Fig. 11. Internal microstructure of SLM Ti6Al4V after nitriding at 900 °C, 15 min. (**a**) SEM microstructure of S11 sample nitrided in SF, (**b**) SEM microstructure of S21 sample nitrided in EF, (**c**) LOM microstructure of S21 sample nitrided in EF.

Nitriding in EF at 1050 °C for 15 min (Fig. 20a–e) induced a color change in sample S18 to light brown, as observed following oxide layer removal (Fig. 20a). LOM and SEM analyses of the cross-section (Fig. 20b, c) distinctly reveal the presence of a discontinuous layer, with areas similar to those identified in Fig. 14a, label C. According to line scan analysis (Fig. 20d,e), these areas contain an average percentage of 2.4% N_2. These areas could be considered as the beginning (initial stage) of compound layer formation.

Figure 21a,b presents the XRD patterns of SLM Ti6Al4V samples subjected to nitriding at 1050 °C for 15 min, carried out in both SF (Fig. 21a) and EF (Fig. 21b). The α-Ti phase is detected in both samples. XRD for the nitrided SF sample (Fig. 21a) confirms the presence of face-centered cubic (FCC) TiN peaks (identified $2\theta \approx 42.25$) and the tetragonal TiN peaks (identified $2\theta \approx 73.8$ and 50, respectively). Also, in this XRD profile (Fig. 21a) it can be seen that the α-Ti peaks were shifted to smaller angles, because of the diffusion of nitrogen atoms in the titanium lattice. These findings are consistent with[54,55]. In the published studies[1,2] the formation of nitrogen compound layers (TiN) and diffusion zone (nitrogen in solid solution, α-Ti(N)) was after holding times of at least one hour[8,56]. In the research presented in[2], during the nitriding of Ti6Al4V manufactured by SLM, at 1050 °C, the compound layer was identified after a holding time of 2 h. While nitriding in SF, using CSE, at 1050 °C, nitrogen compound layers were formed after only 5 min. The formation of this phase, with thicknesses similar to or greater than those obtained after holding times (in conventional furnaces) of over an hour, leads to the conclusion that the gas nitriding thermochemical process, using CSE, is accelerated by the solar radiation[14,57]. The XRD pattern shown in Fig. 21b, for nitriding in EF, indicates no TiN peaks. Instead, the oxide phase of Ti, TiO_2 (rutile) is identified. These findings are in line with results published in[2,5] and[14,45]. The XRD analysis reveals dominant diffraction peaks corresponding to rutile (TiO_2), indicating significant oxide formation on the surfaces of samples nitrided in EF. This result confirms the presence of surface oxidation, which is attributed to titanium higher chemical affinity for oxygen compared to nitrogen, even though the same nitriding conditions as in SF were applied. According to[44,58] α-phase forms rutile rapidly in the presence of oxygen. It is well known that anatase is the metastable phase of TiO_2 and rutile is the thermodynamically stable structure[59,60]. According to the literature[59,61], anatase has a lower thermal stability than rutile and can be converted into rutile at temperatures of 600–700 °C, 1000 °C[62,63] or higher.

The diffractogram, after nitriding for 15 min, at 1050 °C (Fig. 21a), confirms the presence of the metastable phase, anatase, even though the temperature is high. Previous studies[64,65] demonstrated that the transformation of the anatase into rutile, in addition to time and temperature, could be influenced by factors such as the shape of the particles, the presence of {112} facets[66], impurities, manufacturing methods and sample preparation, heating rate, holding time, atmosphere[67,68]. It has also been demonstrated that the thermodynamic stability is dependent on the particle size and anatase can be more stable than rutile when the crystal diameters are smaller than about

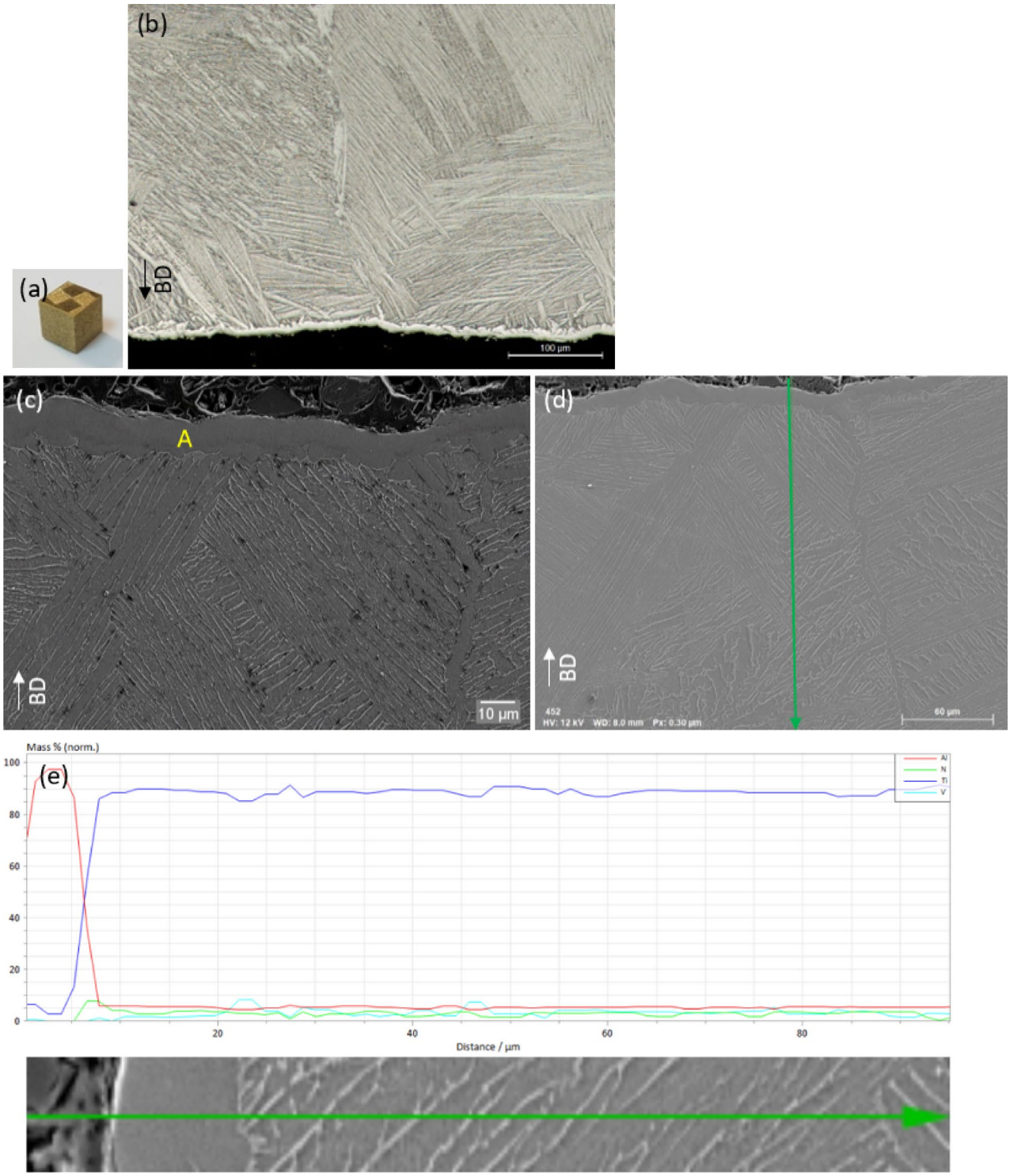

Fig. 12. Gas nitriding at 1050 °C for 5 min in solar furnace. (**a**) sample S12 after nitriding in SF, (**b**) cross-section microstructure from LOM on top part of the sample, (**c**) SEM image on the top part of S12 sample, (**d**,**e**) line scan SEM–EDS analysis on the top of S12 sample cross-section.

14 nm[66]. Based on the previous discussion, the transformation of anatase to rutile during nitriding in SF of SLM Ti6Al4V alloy using CSE could have been influenced by some of the factors aforementioned. This aspect could be an interesting topic for future research, taking into account that the anatase phase has better photocatalytic activity[67,69] and preserving or promoting its formation is desirable.

As expected, the temperature and holding time used for nitriding in both SF and EF also resulted in transformation of the α′ martensite phase (Fig. 22a,b). The micrographs show that the internal microstructure

Treated	Sample code	Temperature [°C]	Holding time [minutes]	Thickness compound layer [µm]	Microhardness, HV		
					Compound layer	Area where should be compound layer	Substrate
Untreated	S0						368.87 ± 29.82
Solar furnace	S10	900	5	–		378.20 ± 35.61	
	S4		10	–		404.83 ± 34.16	
	S11		15	–		430.03 ± 44.21	
	S12	1050	5	10.73 ± 1.35	487.15 ± 45.60		
	S5		10	11.96 ± 2.85	570.73 ± 16.45		
	S13		15	12.73 ± 1.65	625.85 ± 32.98		
	S14	1200	5	17.93 ± 1.35	576.63 ± 55.85		
	S7		10	21.18 ± 2.50	735.70 ± 23.25		
	S15		15	23.35 ± 2.35	813.23 ± 37.47		
Electric furnace	S19	900	5	–		523.23 ± 32.28	
	S20		10	–		658.56 ± 54.63	
	S21		15	–		566.90 ± 31.43	
	S16	1050	5	–		578.78 ± 21.45	
	S17		10	–		527.50 ± 37.09	
	S18		15	–		577.03 ± 12.93	
	S23	1200	5	–		653.33 ± 30.98	
	S22		10	–		613.70 ± 37.62	
	S24		15	–		593.83 ± 6.32	

Table 3. Average values of compound layer thickness and microhardness.

of the SF nitrided sample (Fig. 22a) is lamellar with continuous β-phase and coarse lamellae. The colonies are also larger due to the slow cooling in the furnace. Instead, after the thermochemical treatment of nitriding in EF (Fig. 22b), the microstructure is bi-modal (duplex) with areas where the β-phase is lamellar, continuous and very well defined (high content of V, coarse lamellar), areas with discontinuous lamellar β-phase (thin lamellar) and also areas where the β-phase is in the initial phase of formation (mixture of α and very thin/particles of β-phase) (Fig. 22b, label A).

SEM micrographs reveal coarsening[40] of the α lath as well as growth of the β-phase. In comparison to the β-phase in the samples nitrided at 900 °C, after nitriding at 1050 °C and 1200 °C, the β-phase shows a more organized and directed pattern[70], particularly in the samples nitrided in SF and on certain areas of those nitrided in EF. These results are in line with the previous studies[71,72]. In addition, equiaxed α grains were observed only after 15 min, at 1050 °C (Figs. 19c and 20c). Figure 23a–e shows the sample (S14) and the results of the LOM, SEM analyses after the gas nitriding in SF, at 1200 °C, for 5 min. Increasing the nitriding temperature determined both the increase in the thickness of the nitrogen compound layer (Fig. 23b,c) (an average of 17.93 ± 1.35 µm, Table 3) and its nitrogen concentration to an average of 4.07% (Fig. 23d–e). Increasing the concentration of N_2, after a holding time of 5 min, also determined the increase in microhardness (Table 3). These results are consistent with previously published results[14,28].

Nitriding in EF, at 1200 °C, for 5 min, revealed, as in the previous EF nitridings, the occurrence of oxidation, which led to the deposition of an oxide layer onto the sample surface (Fig. 24a–e) and, consequently, influenced the process nitriding. SEM micrographs of the sample cross-section (Fig. 24c–e) indicate that, even after the temperature of 1200 °C, no nitrogen compound layer is present (Table 3), in contrast to the layer formed under identical conditions in SF (Fig. 23c–e). Instead, a layer enriched in aluminum (label B in Fig. 24c–e) was identified beneath the oxide layer. This Al-rich layer was observed to increase in thickness with longer holding times. The line scan SEM–EDS analysis (Fig. 24d,e) confirms the presence of the oxide layer. Also, the high content of Al, in the layer labeled B, is confirmed both by the line scan analysis (Fig. 24d,e) and by the one in spectrum 1 in Fig. 25.

The formation of this layer, which was also identified in studies published by other researchers[45,73], can be caused by the presence of oxygen, which, like nitrogen, is an α-phase stabilizer. It is well known that oxygen has a large solubility in α-Ti (HCP phase) compared to β-Ti (BCC phase). Diffusion of oxygen in the Ti substrate (through the oxide scales) can lead to an increase of the α-phase proportion (as α-phase stabilizer) because of it can transform the β-phase into the α + β phase or into the total α-phase, according to[45].

During nitriding in SF, no gray brittle layers was deposited on the samples (through XRD analysis, only a weak signal associated with anatase was identified) most likely due to the atmosphere in SF contained a very small amount of oxygen and nitrogen had high purity. The acceleration of the nitriding process under solar radiation, as noted in[37], likely contributed to enhanced nitrogen uptake. The resulting nitrided layer significantly improved the oxidation resistance of the SLM Ti6Al4V alloy, acting as an effective protective barrier against oxygen ingress into the substrate[7,74].

The temperatures of thermochemical treatments consistently induced modifications in the core microstructure of the SLM Ti6Al4V alloy, transforming the initial acicular martensite into α and β lamellae

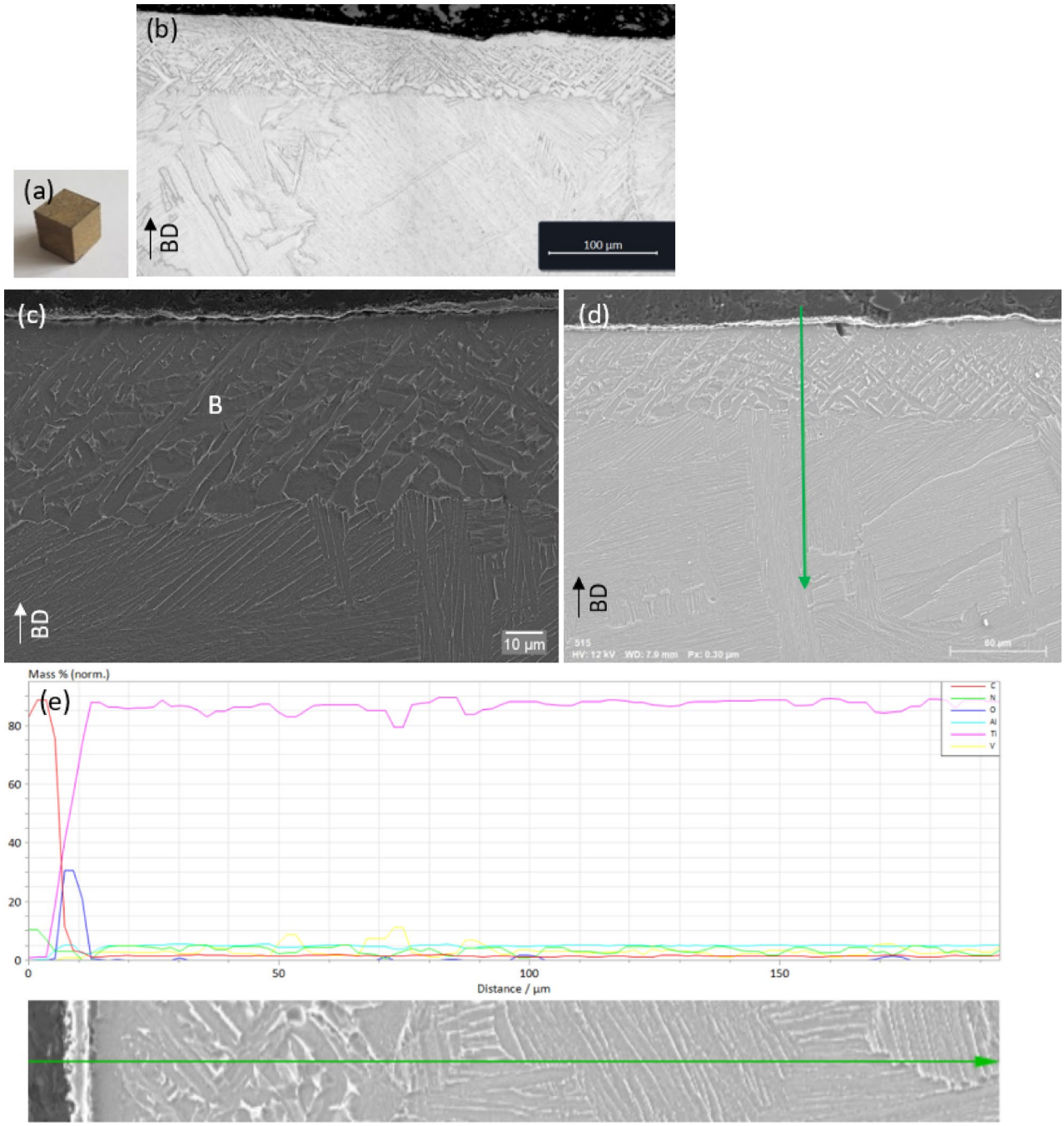

Fig. 13. Gas nitriding of S16 sample, at 1050 °C for 5 min in electric furnace. (**a**) sample S16 after nitriding, (**b**) OM of cross-section microstructure on top part of the sample, (**c**) SEM image on the top part of S16 cross-section, (**d**,**e**) line scan SEM–EDS analysis on the top of S16 cross-section.

with various morphologies[2], including Widmanstätten and bimodal microstructures. Nitriding at 1200 °C in SF promoted the conversion of martensite into Widmanstätten structure in areas situated at certain depths from the outer nitrided surfaces (Fig. 26a), while the areas inside the sample exhibited a lamellar α + β phase. The high processing temperature also determined coarsening of the α-phase (Fig. 26b) inside the coarsened grains. After nitriding in EF, the microstructure is a mixture of α phase colonies, with α-phase coarsened, and areas with thin lamellar β-phase and very small particles (Fig. 26c,d).

Increasing the holding time to 10 min during gas nitriding in SF led to an intensified nitriding process, as evidenced by an increase in the average thickness of the nitrogen compound layer to 21.18 ± 2.50 µm (Fig. 27b,c; Table 3) and a corresponding rise in nitrogen content to an average of 4.5%, based on SEM–EDS analysis (Fig. 27d,e). This enhanced nitrogen diffusion is confirmed by the darker golden color of sample S7 (Fig. 27a),

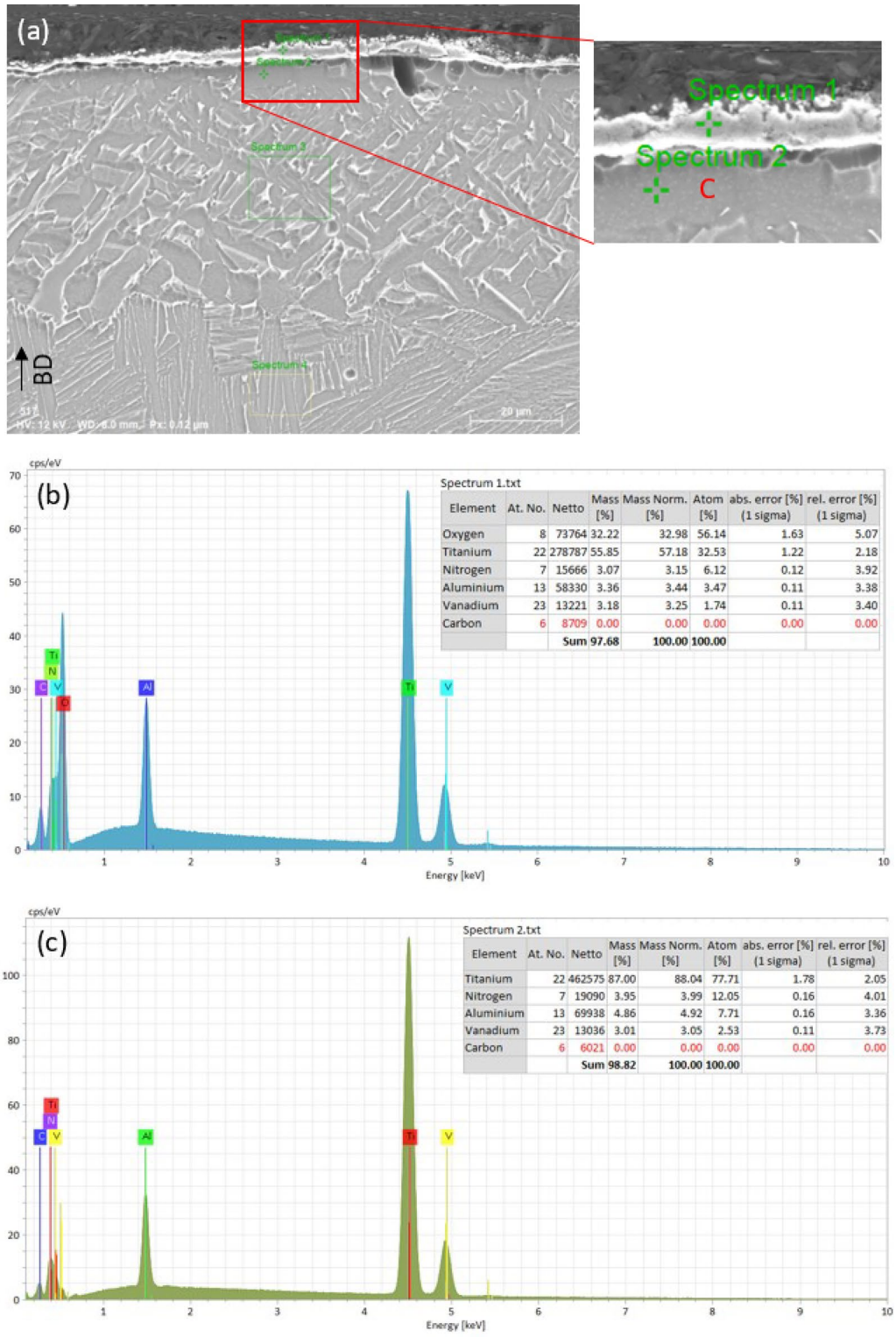

Fig. 14. SEM–EDS spot analysis and quantification results. (**a**) spectrum 1 on the cross-section of S16 sample; (**b**) elemental peak intensities of the spectrum1; (**c**) elemental peak intensities of the spectrum2.

in comparison to the 5 min nitrided sample (Fig. 23a). Additionally, the microhardness of the compound layer increased significantly, reaching an average value of 735.7 ± 23.25 HV (Table 3).

Gas nitriding in EF at 1200 °C after 10 min did not result in the formation of a nitrogen compound layer, as indicated in Table 3 and illustrated in Fig. 28a–e. This contrasts with the results under identical thermal conditions in SF, where compound layer was formed. An increase in the thickness of the Al—rich layer (Fig. 28c–e) is evident beneath the O_2—rich layer (Fig. 2e). The area that can be similar to the diffusion zone (Fig. 28c)

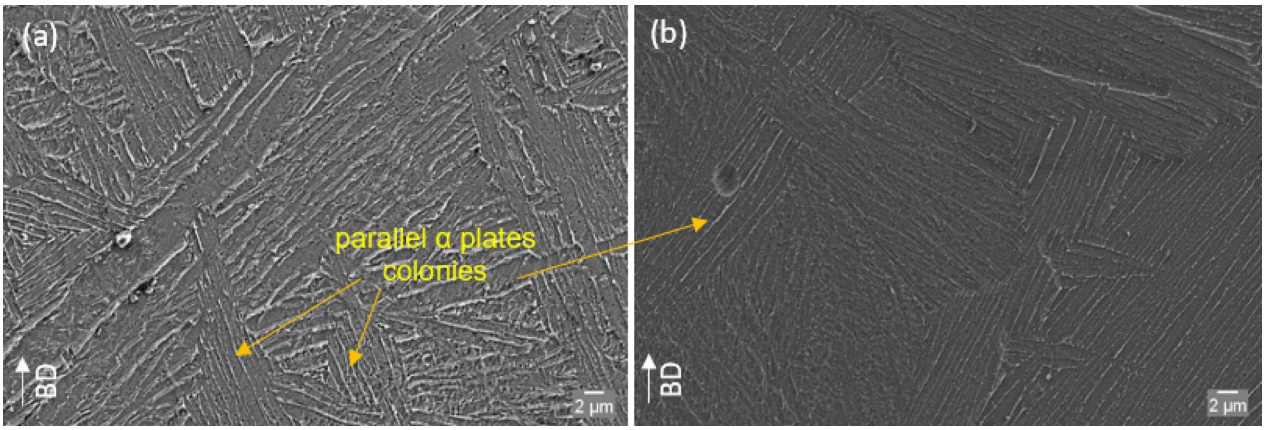

Fig. 15. Internal microstructure of SLM Ti6Al4V after nitriding at 1050 °C, 5 min. (**a**) SEM microstructure of S12 sample nitrided in SF; (**b**) SEM microstructure of S16 sample nitrided in EF.

appears slightly reduced in width but exhibits a higher density of equiaxed α-phase, while the volume fraction of β-phase decreased. As previously explained and corroborated with published studies[45,76], nitrogen, as oxygen, is a stabilizing alloying element for α-Ti and nitrogen dissolved in the β-phase (β-Ti) transform the β-phase into α-Ti. These transformations are substantiated by the decrease in microhardness compared to the sample microhardness subjected to 5 min holding time, as well as in samples treated under similar conditions in SF.

As shown in Fig. 29a,b, the internal microstructure consists of α + β lamellae grouped in colonies with the same orientation. As highlighted in the literature[39,40], this is the typical result for the heat treatment in which the slow cooling rate is applied. It is also known that high ductility values of titanium are associated with the lamellar α + β microstructure, where the α laths are grouped in colonies[76,77]. Considering the high temperature, even though the holding time was only 10 min, in the areas close to the nitrogen compound layer (Fig. 27c,d) or the outer surface (Fig. 28c) it is found the formation of the coarsened equiaxed α—phase as well as the Widmanstätten structure.

Nitriding in SF at 1200 °C, for 15 min (Fig. 30a–e), increased the nitrogen concentration in the compound layer to 5% (Fig. 30d,e). The darker golden color of the sample (Fig. 30a) confirms the presence of the nitride layer whose average thickness has increased to 23.35 ± 2.35 µm (Fig. 30b,c; Table 3). SEM–EDS maps of chemical components (Ti, Al, V, N) distribution performed on the cross-section of S15 sample, in Fig. 31a–e are presented. The high nitrogen content of the compound layer is also revealed in its distribution map (Fig. 31c) as well as by the high value of its microhardness of 813.23 ± 37.47 HV (Table 3). As mentioned previously, it is difficult to clearly differentiate between nitrogen and titanium because the N-Kα spectrum overlaps with that of Ti and, consequently, it is possible that the nitrogen inside the mapping area is not accurate, as was highlighted in references[5,47]. Figure 31e) shows a low distribution of vanadium within nitrogen compound layer, indicating its inward migration and diffusion zone. This redistribution contributes to an increased fraction of the β-phase and a corresponding increase in vanadium content within this area, phenomenon confirmed by the SEM–EDS peaks in Fig. 30e).

Holding time of 15 min in EF resulted in the formation of an oxide layer on the surface of the S24 sample (Fig. 32a–e), accompanied by an increase in aluminum concentration underneath this oxide layer (from 7.4% after 5 min to 11.2% at 15 min) (Fig. 32d–e). Simultaneously, a reduction in vanadium content was observed, a trend confirmed by the elemental distribution in the SEM–EDS maps (Fig. 33a–f). Nitrogen content within the Al-rich layer is low and exhibited an inverse correlation with the holding time, decreasing from 0.86% at 5 min to 0.69% at 10 min, and further to 0.48% at 15 min. This decrease confirms that oxygen is absorbed faster by the SLM Ti6Al4V ELI alloy and the oxide layer acts as a barrier in the nitriding process.

The internal microstructure of samples nitrided at 1200 °C for 15 min confirms the transformation of acicular martensite α′ into Widmanstätten structure, predominantly lamellar (Fig. 34a–d) with the phase α and β coarsened, particularly during nitriding in SF (Fig. 34a,b). The SF nitrided sample contains, in some areas, basketweave structures and equiaxed α-phase.

The presence of the coarsened, equiaxed α-phase in sample (S24) nitrided in EF, mainly in the areas closer to the outer surfaces (Fig. 32c,d) is attributed to strong ingress of the oxygen into the sample.

Microhardness measurement

The formation of α′ martensite after the selective laser melting of the Ti6Al4V ELI powder contributes to an increase of the alloy hardness[78] compared to Ti6Al4V alloy obtained by conventional processes. The average hardness of the as-fabricated SLM Ti6Al4V was (368.87 ± 29.82) $HV_{0.01}$ which is in accordance with the previous results for Ti6Al4V fabricated by SLM[2,33]. High standard deviation attributed to the martensitic phase and inhomogeneity of the microstructure. These factors are also reported in the studies presented in[2,18]. All gas nitriding treatments resulted in an increase of the samples surface hardness (Table 3), accompanied by a progressive decrease in hardness from the treated surface toward the bulk material. The highest surface hardness, of 838.7 HV, was measured on the compound layer after nitriding in SF, at 1200 °C, with a holding time of 15 min.

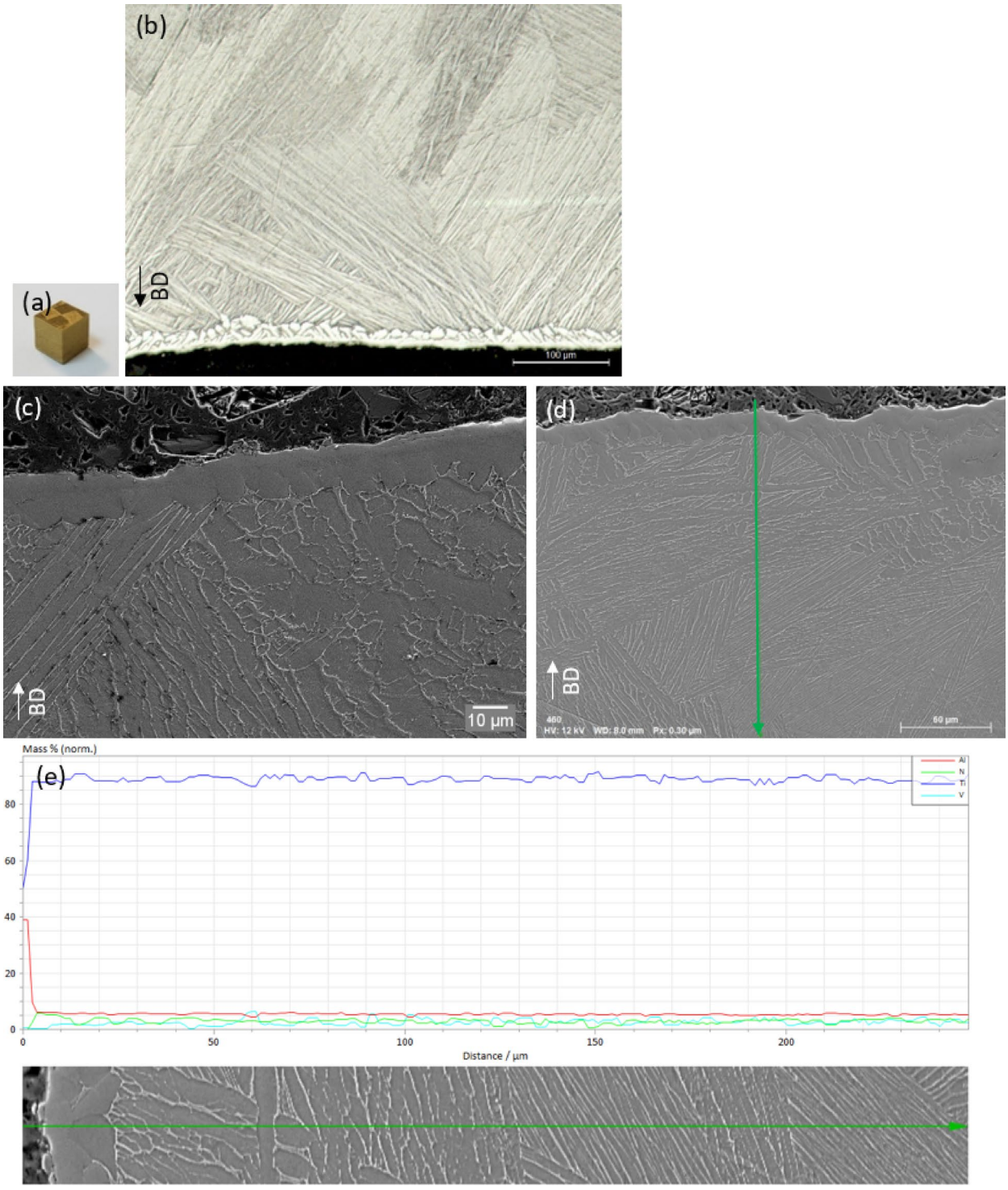

Fig. 16. Gas nitriding at 1050 °C for 10 min in solar furnace. (**a**) sample S5 after nitriding in SF, (**b**) cross-section microstructure from LOM on top part of the sample, (**c**) SEM image on the top part of S5 sample, (**d**,**e**) line scan SEM–EDS analysis on the top of S5 sample cross-section.

The average value of the microhardness corresponding to the five measurements on the compound layer is 813.23 ± 37.47 HV (Fig. 36a). As shown in Fig. 35a the hardness of the area in the upper part of the cross-section of the sample nitrided at 900 °C, in SF, is slightly higher than substrate (also higher than the hardness of the as-fabricated Ti6Al4V ELI alloy). At temperature of 900 °C, the compound layer well delimited by the substrate is still not formed (Figs. 3, 6, and 9) and this increase in microhardness confirms that nitrogen diffusion in the SLM Ti6Al4V alloy has taken place. The hardness of the samples substrate, nitrided in SF, shows a slight decrease compared to the hardness of the as-fabricated sample (S0). This decrease was due to increasing of alpha-Ti grains

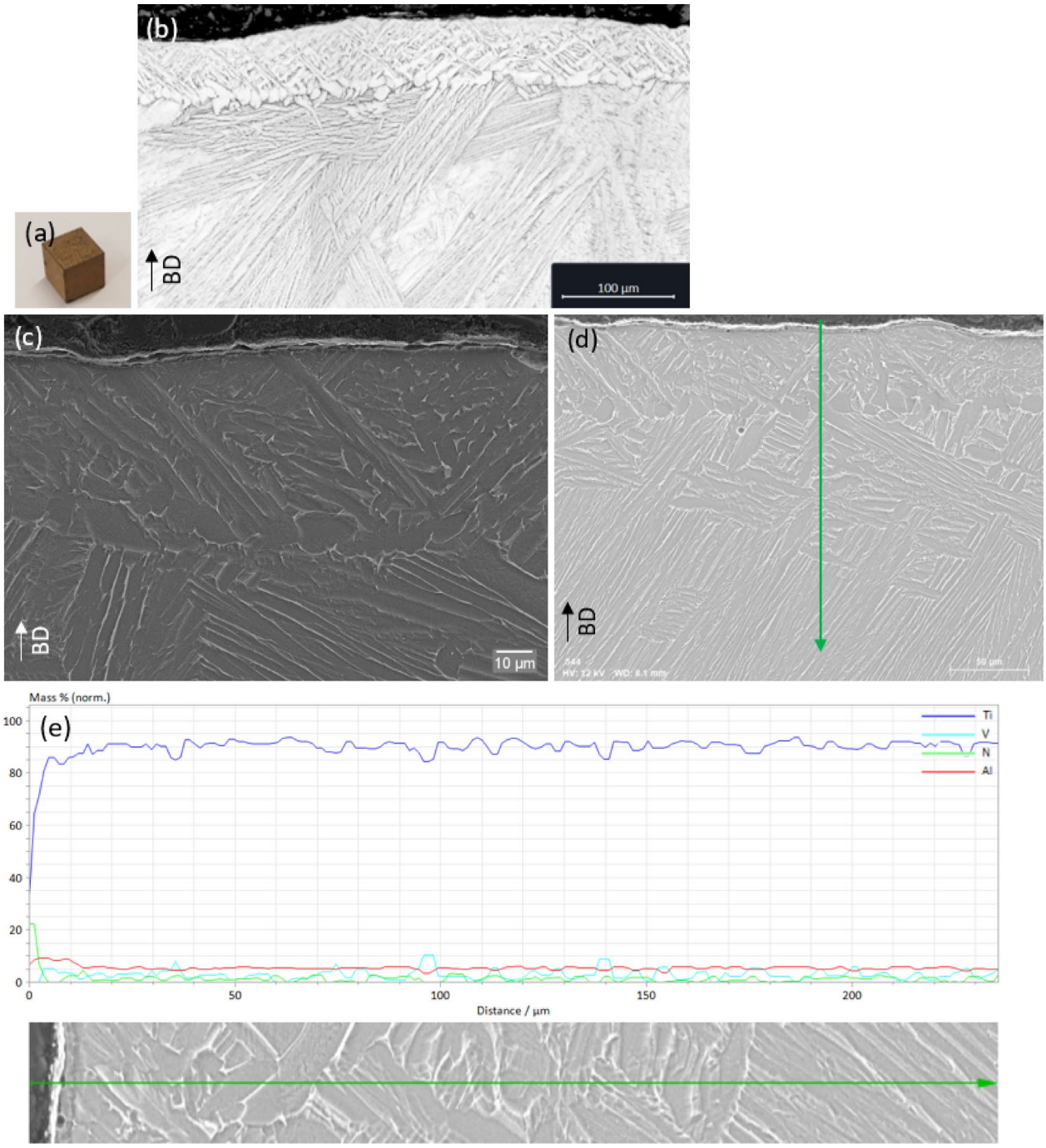

Fig. 17. Gas nitriding of S17 sample, at 1050 °C for 10 min in electric furnace. (**a**) sample S17 after nitriding, (**b**) OM of cross-section microstructure on top part of the sample, (c) SEM image on the top part of S17 cross-section, (**d**,**e**) line scan SEM–EDS analysis on the top of S17 cross-section.

compared to the microstructure of the non-thermochemically treated samples (S0), which presents a thinner microstructure (α′ martensite). Towards the inside of the sample, the microhardness approaches that of the S0 sample (untreated) because of the microstructure still contains α′ martensite. These findings are in line with[9,40]. Figure 35b, microhardness profile after nitriding in EF, shows a significant increase in hardness in the upper part of the sample cross-section compared to the hardness of the untreated one (S0) (Table 3). It is also higher than that obtained after nitriding in SF (Fig. 35a).

The high microhardness observed in the samples nitrided in the EF (Figs. 35b, 36b, 37b) is attributed to the increased oxygen content[2] and the presence of an oxide layer, as was previously demonstrated in this work, which influenced the nitriding process in EF. Consequently, it is considered that it would not be appropriate to compare the microhardness of the samples nitrided in SF with those in EF. Microhardness profile of samples nitrided

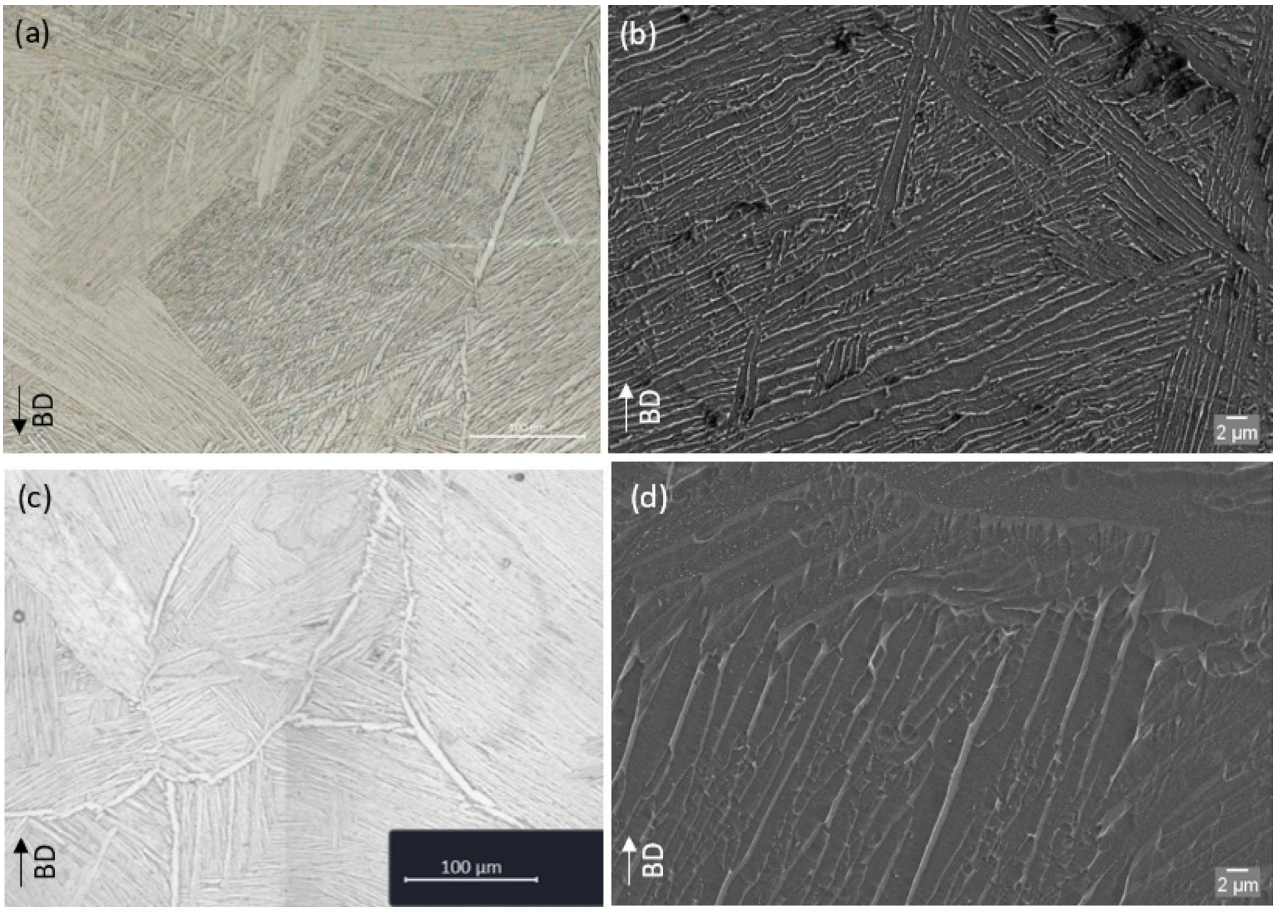

Fig. 18. Internal microstructure of SLM Ti6Al4V after nitriding at 1050 °C, 10 min. (**a**,**b**) LOM and SEM microstructure of S5 sample nitrided in SF; (**c**,**d**) LOM and SEM microstructure of S17 sample nitrided in EF.

at 1200 °C, in SF, in Fig. 36a is presented. As previously demonstrated, the temperature of 1200 °C resulted in an increase in the thickness (Table 3) and nitrogen concentration of the compound layer, and therefore to the increase of its hardness with the increase of holding time.

Despite the shorter holding times, an increase in microhardness was also observed in the underneath (nitrogen diffusion zone) of the nitrided layer. This microhardness progressively decreases with increasing depth from the surface toward the interior, further confirming a corresponding decrease in nitrogen concentration from the compound layer to the bulk material.

The average values of the microhardnesses measured on nitrogen compound layers related to the holding times of 5, 10 and 15 min respectively, at 1200 °C, in SF, were 576.63 ± 55.85 HV, 735.70 ± 23.25 HV and respectively 813.23 ± 37.47 HV (Table 3). Figure 37a,b shows microhardness profiles obtained after a holding time of 10 min at nitriding temperatures of 900, 1050, and 1200 °C. An increase in nitriding temperature from 900 to 1050, and 1200 °C respectively (holding time of 10 min) resulted in a visible increase in the thickness of the nitrogen compound layer (Fig. 38a–c, and Table 3) as well as an increase of the microhardness (Fig. 37), findings that stand in contrast to the assertions made in reference[36].

Holding for only 10 min at 900 °C led to the increase of the microhardness of the nitrogen diffusion zone, from 351.3 ± 17.84 HV (the microhardness average value of the substrate which is very close to that of the as-fabricated microstructure, 368.87 ± 29.82), to 404.83 ± 34.16 HV (Table 3). Increasing the temperature to 1050 °C and 1200 °C respectively, at the same holding time, determined the formation of the nitrided layer (Fig. 38b,c) and also the increase of its microhardness to 570.73 ± 16.45 HV (compared to the average value of the substrate of 426.23 ± 45.10 HV) and respectively 735.70 ± 23.25 HV (with the microhardness of the substrate of 464.40 ± 35.87 HV) (Table 3).

Comparing the microhardness measured after SLM Ti6Al4V ELI nitriding in SF (Figs. 36a and 37a) and EF (Figs. 36b and 37b) (Table 3), it was found that most of them are higher after nitriding in SF even though the surface and microstructure of the samples after nitriding in EF contains a high percentage of oxygen. However, the quickly formed oxide layer on the surface of the samples acted as a barrier to the diffusion of nitrogen but also to the subsequent diffusion of oxygen in the upper layers. To date, the available literature on the gas nitriding of Ti6Al4V ELI alloy produced by SLM remains scarce. Furthermore, no studies have been identified that specifically investigate the gas nitriding of SLM Ti6Al4V in a solar furnace using CSE. As mentioned, and demonstrated previously, it is well known that the microstructure of the SLM Ti6Al4V alloy is completely

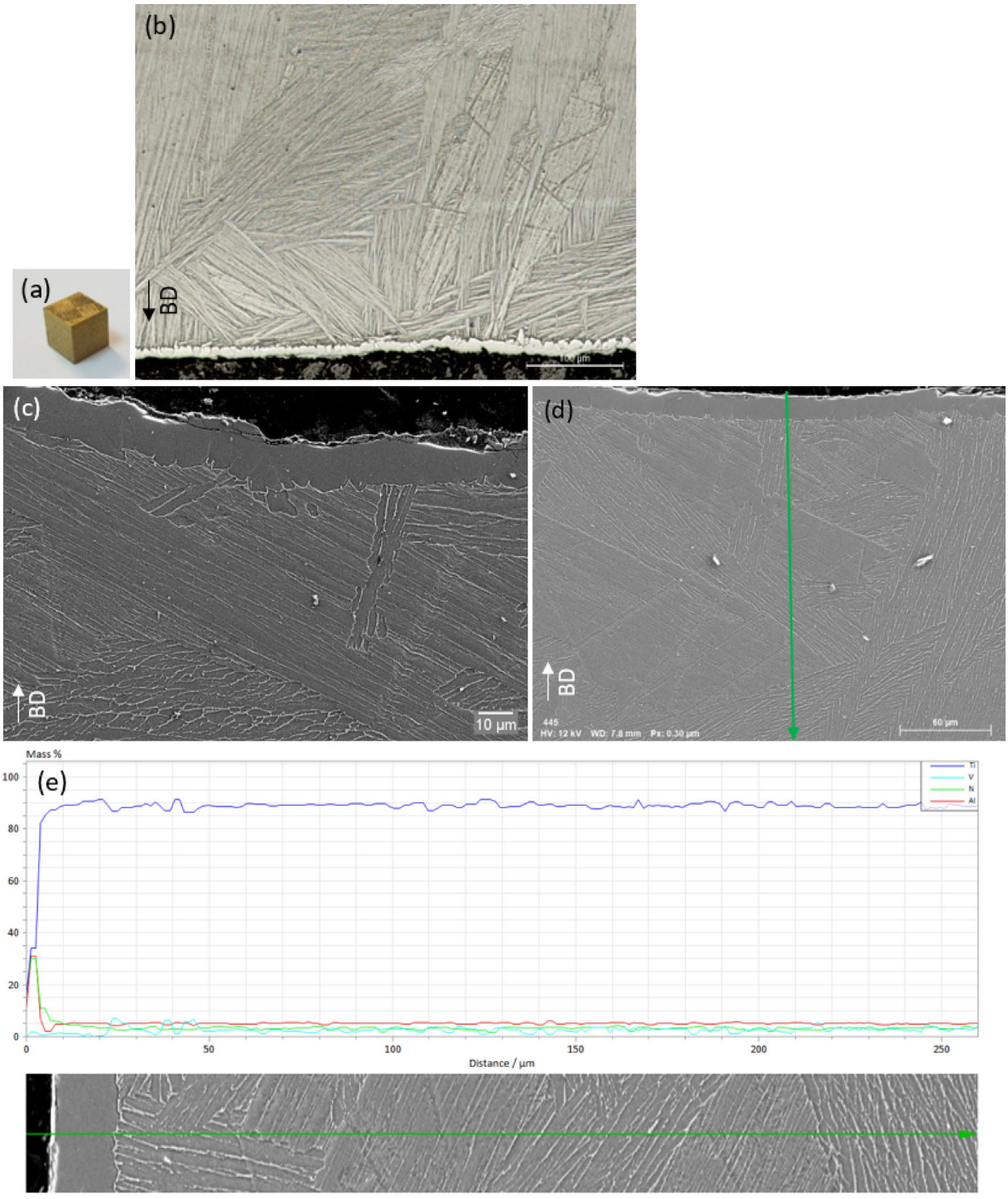

Fig. 19. Gas nitriding at 1050 °C for 15 min in solar furnace. (**a**) sample S13 after nitriding in SF, (**b**) cross-section microstructure from LOM on top part of the sample, (**c**) SEM image on the top part of S13 sample, (**d**,**e**) line scan SEM–EDS analysis on the top of S13 sample cross-section.

different from the alloy obtained by conventional processes and as a consequence the SLM Ti6Al4V alloy behaves differently to the conventional thermal and thermochemical treatments applied to the Ti6Al4V alloy manufactured by classical processes, as also stated in[33,79]. Valente et al.[2], in their research, after gas nitriding in the electric furnace, at 1050 °C, of Ti6Al4V manufactured by SLM, indicated a hardness, measured at a depth of 20 µm from the sample surface, of 772 ± 65 HV but after a holding time of 2 h. According to the authors[2], the highest hardness, of 963 ± 52 HV, was obtained after nitriding at a temperature of 1000 °C, also at a depth of 20 µm. But this microhardness value was obtained after a holding time of 16 h. Kao et al.[1], after gas nitriding, at

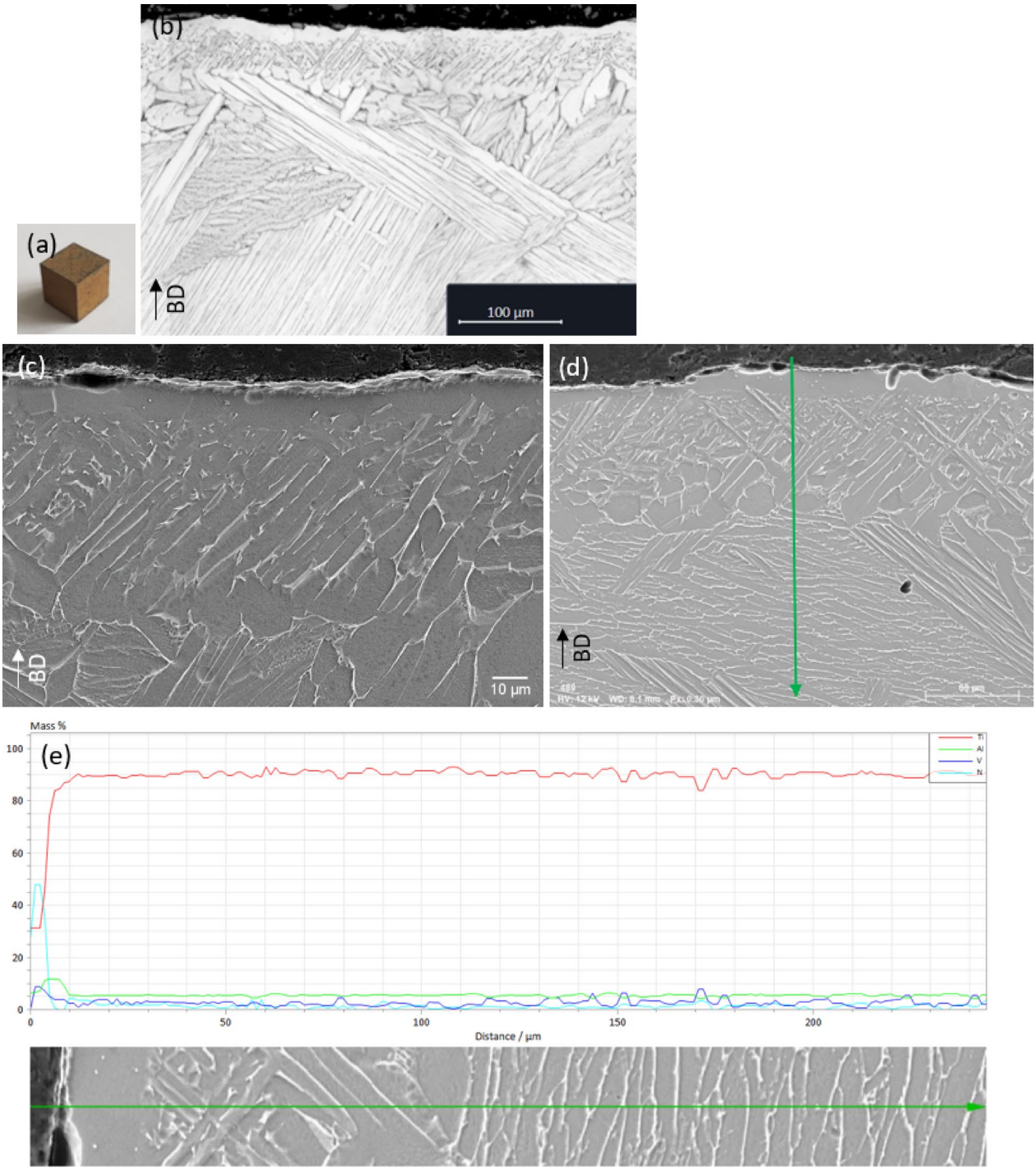

Fig. 20. Gas nitriding of S18 sample, at 1050 °C for 15 min in electric furnace. (**a**) sample S18 after nitriding, (**b**) OM of cross-section microstructure on top part of the sample, (**c**) SEM image on the top part of S18 cross-section, (**d**,**e**) line scan SEM–EDS analysis on the top of S18 cross-section.

900 °C, for 160 min, in the electric furnace, of the SLMed Ti6Al4V, obtained a hardness of 776 ± 9 HV. In this research the nitriding of SLMed Ti6Al4V ELI in SF, for only 15 min, led to the increase of the microhardness in the nitrogen diffusion zone to 430.03 ± 44.21 HV (Table 3, Fig. 35a), more than half of the microhardness obtained in the research presented in[1].

In the studies published in[14,15], after gas nitriding of Ti6Al4V alloy manufactured by conventional methods (mill-annealed and with α + β microstructure), for 15 min, at 1200 °C, using Fresnel lens and respectively 1000 °C in SF, microhardness of 2100 HV[14] and 1400 HV respectively were reached. In the present work, after nitriding in SF, microhardness close to those mentioned in[14,15] was not reached. The maximum hardness obtained after nitriding in SF at 1200 °C, for 15 min, was 838.7 HV. This can be explained by the fact that, as previously

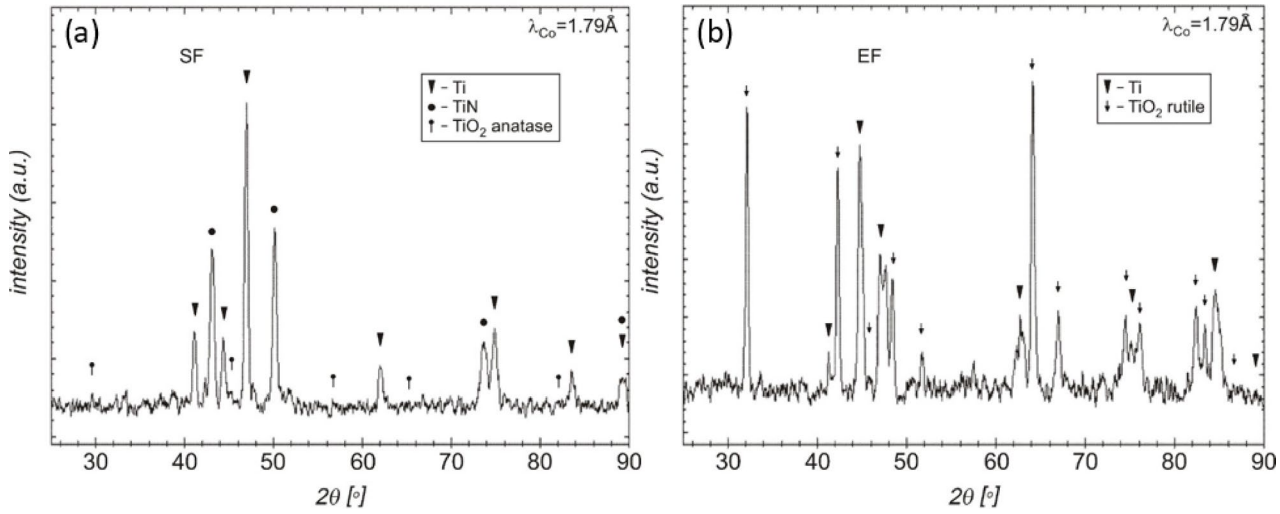

Fig. 21. XRD analysis of SLM Ti6Al4V samples gas nitrided at 1050 °C for 15 min. (**a**) XRD for sample nitrided in SF, (**b**) XRD for sample nitrided in EF.

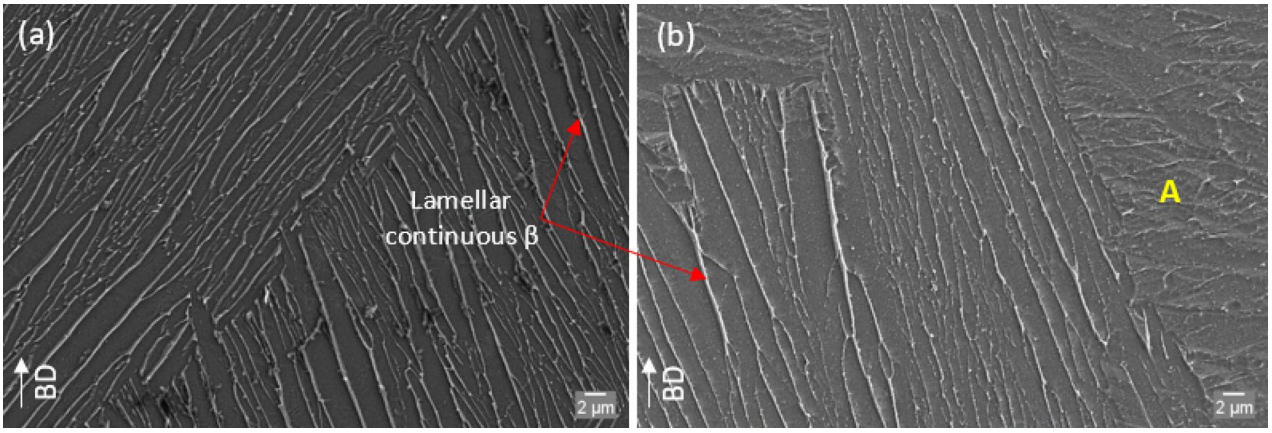

Fig. 22. Internal microstructure of SLM Ti6Al4V after nitriding at 1050 °C, 15 min. (**a**) SEM microstructure of S13 sample nitrided in SF; (**b**) SEM microstructure of S18 sample nitrided in EF.

pointed out, the Ti6Al4V alloy manufactured by SLM behaves totally different from the one obtained by classical processes. To date, the nitriding kinetics of Ti6Al4V alloy produced by SLM has not been investigated. Even more notably, there is a complete absence of published studies addressing the nitriding kinetics of this alloy when treated in SF using CSE.

Heating and processing times

The previously presented results reveal that the gas nitriding thermochemical treatment of SLM Ti6Al4V ELI, using CSE and considerably shorter holding times, led to results similar or at least close to those obtained after nitriding in EF, using conventional energy, but, in these cases, with much longer process times. Obtaining excellent results after gas nitriding, in SF, but in much shorter process times, confirm previous studies[14,37] as well as the authors conclusions that the application of CSE enhances the nitriding process. Specifically, CSE exerts an activating effect that promotes accelerated nitrogen diffusion within the Ti6Al4V alloy produced by SLM.

Figure 39a shows the graphic representation of the heating times calculated as the average value of the heating times (the time until the temperature of 900, 1050, and 1200 °C is reached and then the holding time begins) for the thermochemical nitriding treatments with a holding time of 5, 10, and 15 min. In Fig. 39b the estimated values of the total times (heating, holding, cooling) for each process are represented. The time values were extracted from the data recorded by the SF process monitoring and control software system, SCADA, and regarding the thermochemical nitriding treatment in the electric furnace, the time values were taken from the displayed data by the monitoring and control system of the Nabertherm electric furnace. It is more than obvious from Fig. 39 that the nitriding thermochemical treatment using CSE is much more efficient compared to the one that used conventional energy, in EF. When using CSE in SF, the heating time required for gas nitriding is reduced by up to 74% compared to using conventional energy in EF. In SF, the shortest heating time was 10 min

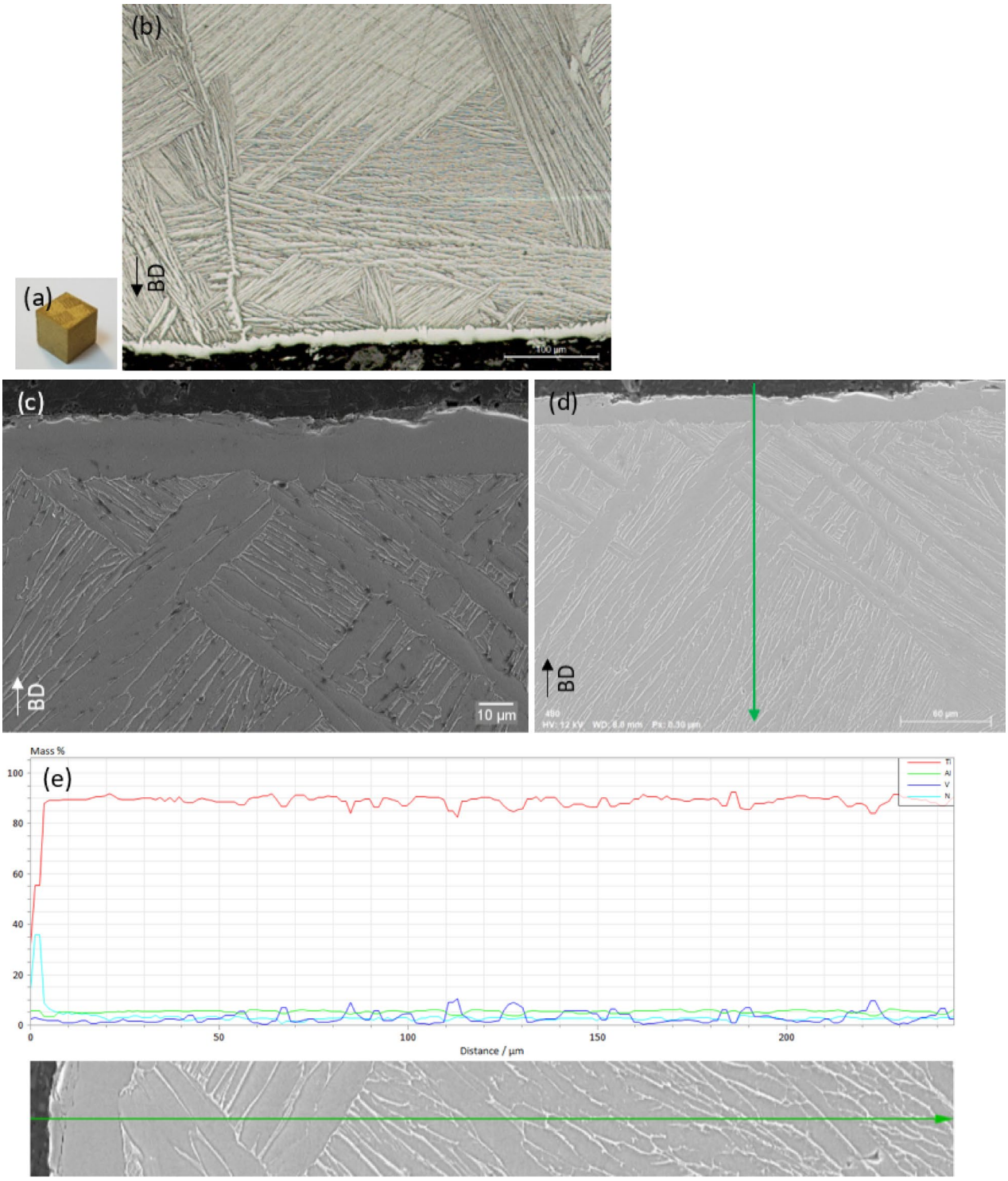

Fig. 23. Gas nitriding at 1200 °C for 5 min in solar furnace. (**a**) sample S14 after nitriding in SF, (**b**) cross-section microstructure from LOM on top part of the sample, (**c**) SEM image on the top part of S14 sample, (**d**,**e**) line scan SEM–EDS analysis on the top of S14 sample cross-section.

to reach the temperature of 900 °C. While in EF, to reach the same temperature, 45 min were needed. The total process times for nitriding in SF are shorter than in EF by up to 73%. In SF, for example, the total time for thermochemical treatment carried out at 1200 °C, for 15 min, is 42 min, while 135 min were required for the same process in EF.

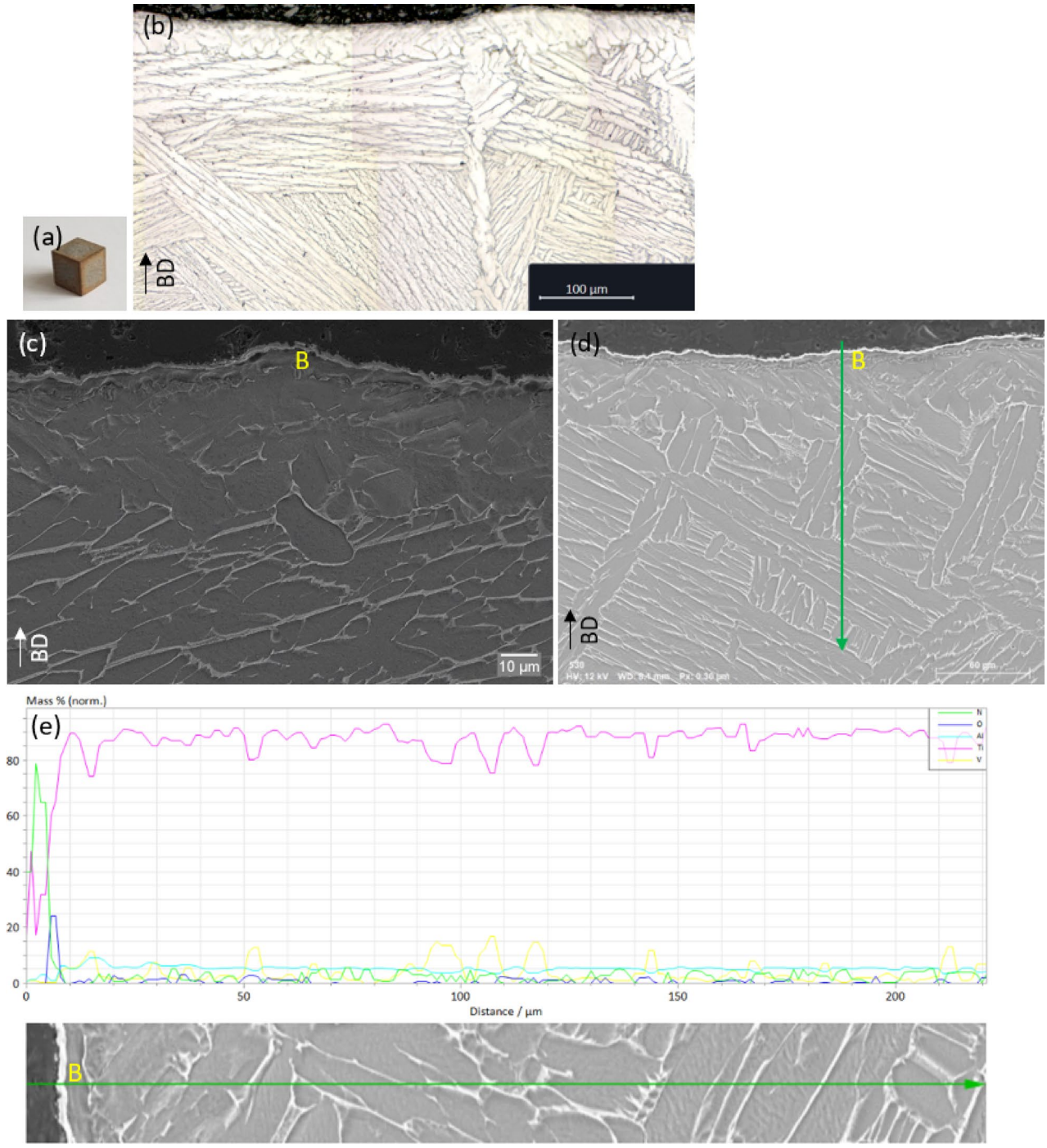

Fig. 24. Gas nitriding of S23 sample, at 1200 °C for 5 min in electric furnace. (**a**) sample S23 after nitriding, (**b**) OM of cross-section microstructure on top part of the sample, (**c**) SEM image on the top part of S23 cross-section, (**d**,**e**) line scan SEM–EDS analysis on the top of S23 cross-section.

Conclusions

Recognized as a sustainable technology, the most important environmental impact that can be attributed to AM is the reduction of resource consumption, waste and pollution. When combined with renewable energy sources like CSE, which has the ability to generate extremely high temperatures in a very short time, the sustainability potential of AM is further enhanced. In this work, the first study is presented regarding the thermal and gas nitriding thermochemical treatment, carried out simultaneously, of the Ti6Al4V alloy manufactured by SLM process, in the solar furnace, using CSE as a source of renewable energy. The main findings are summarized as follows:

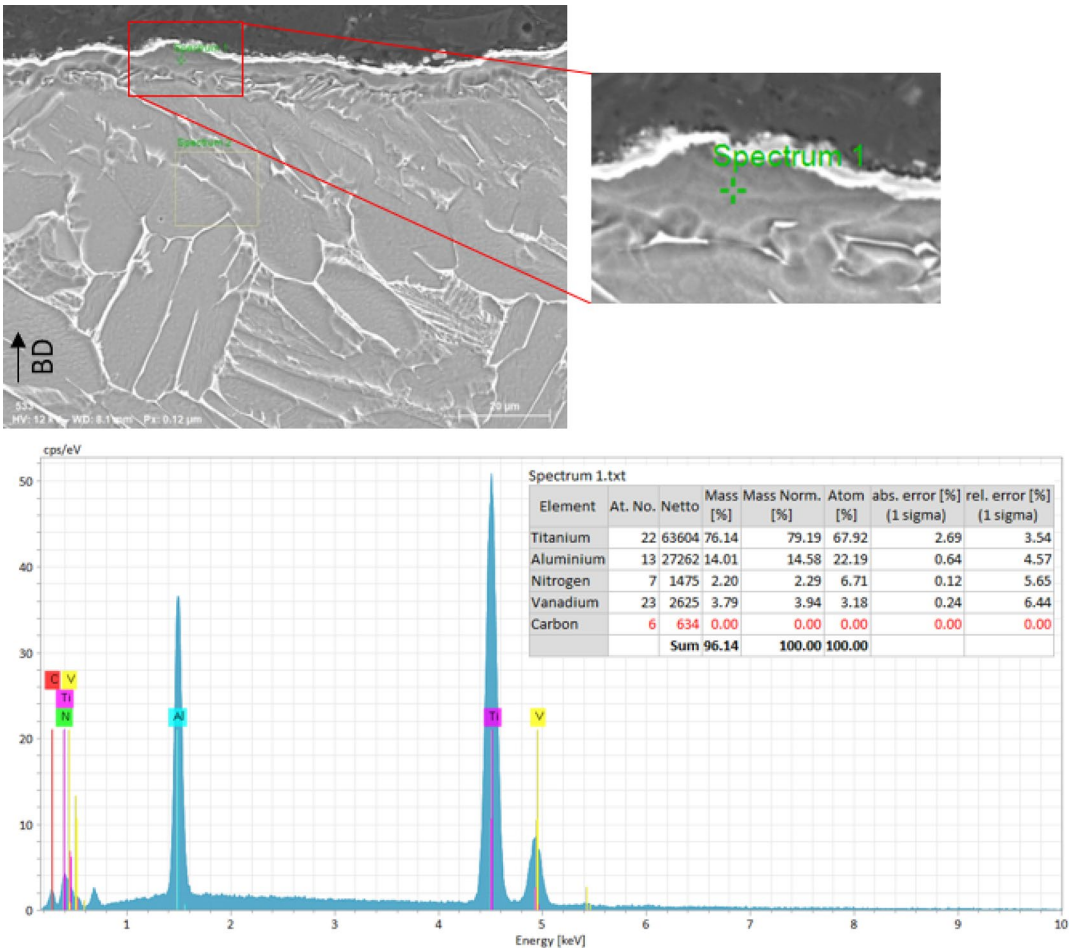

Fig. 25. Spot analysis showing elemental peak intensities of the spectrum1.

1. The results confirmed that CSE can be used as an alternative energy source (green, renewable energy) in post-process, at high-temperatures gas nitriding thermochemical treatments, of the SLM Ti6Al4V alloy.
2. Gas nitriding post-processing using CSE can be completed in considerably shorter time than traditional thermochemical nitriding processes that rely on conventional energy sources such as electric furnaces. When using CSE, the gas nitriding duration is reduced by up to 73% compared to the conventional furnace.
3. Nitriding in SF, using CSE, led to the formation of the nitrogen compound layer and the diffusion zone after short holding times of only 5, 10 and 15 min, respectively.
4. All nitriding treatments conducted in SF led to an increase in the microhardness of the SLM Ti6Al4V alloy. The maximum microhardness, reaching 838.7 HV, was recorded in the compound layer after nitriding at 1200 °C for only 15 min.
5. All gas nitriding thermochemical treatments in SF, even at short holding times, led to the modification of the internal microstructure, transforming the initial α′ martensite into α + β phases of different morphologies and sizes.
6. The application of CSE enabled thermochemical nitriding of the SLM Ti6Al4V alloy at heating and cooling rates of 80 °C/min—significantly higher than conventional furnace maximum of 20 °C/min—thereby reducing the gas nitriding post-process time.
7. The results achieved through short-duration nitriding using CSE confirm that the photoactivation mechanism of titanium alloy nitriding, as outlined in reference[37], also applies to the Ti6Al4V alloy produced by AM emerging technology (particularly, SLM process), even though the nitriding kinetics of such alloy is not very well studied, yet. Therefore, further research is needed to substantiate these findings.

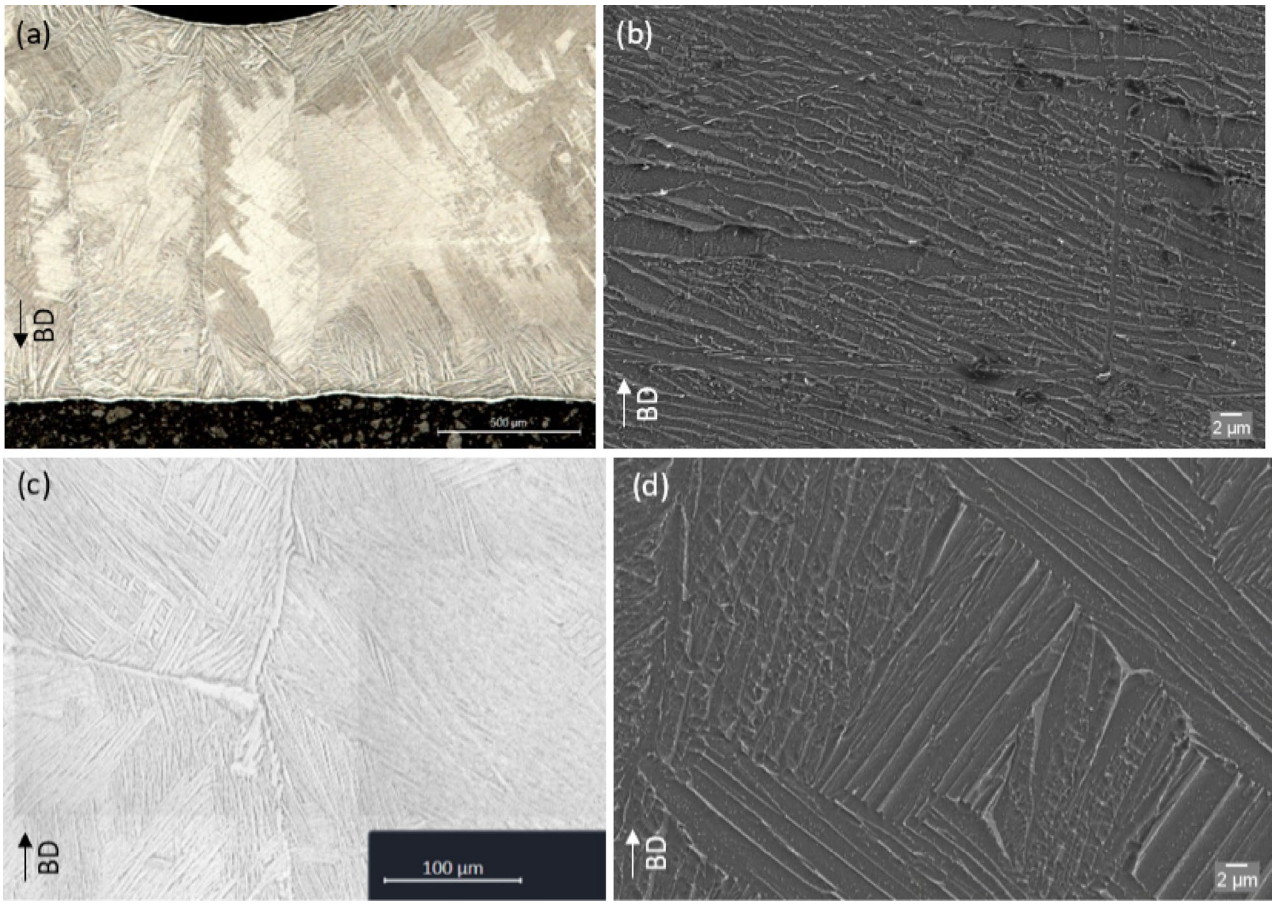

Fig. 26. Internal microstructure after nitriding at 1200 °C, 5 min. LOM and SEM micrographs after nitriding in SF (**a**,**b**) respectively EF (**c**,**d**).

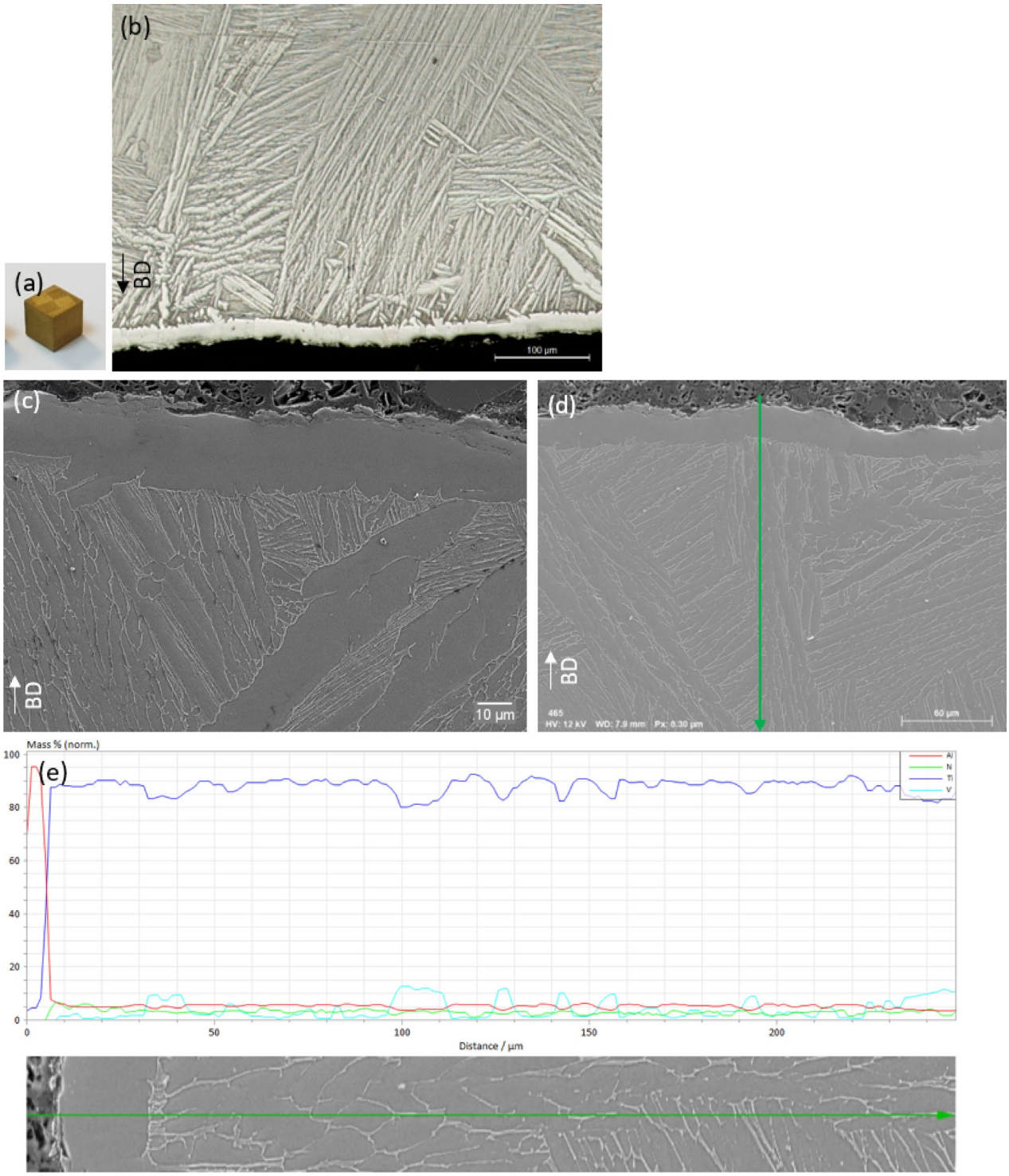

Fig. 27. Gas nitriding at 1200 °C for 10 min in solar furnace. (**a**) sample S7 after nitriding in SF, (**b**) cross-section microstructure from LOM on top part of the sample, (**c**) SEM image on the top part of S7 sample, (**d**), (**e**) line scan SEM–EDS analysis on the top of S7 sample cross-section.

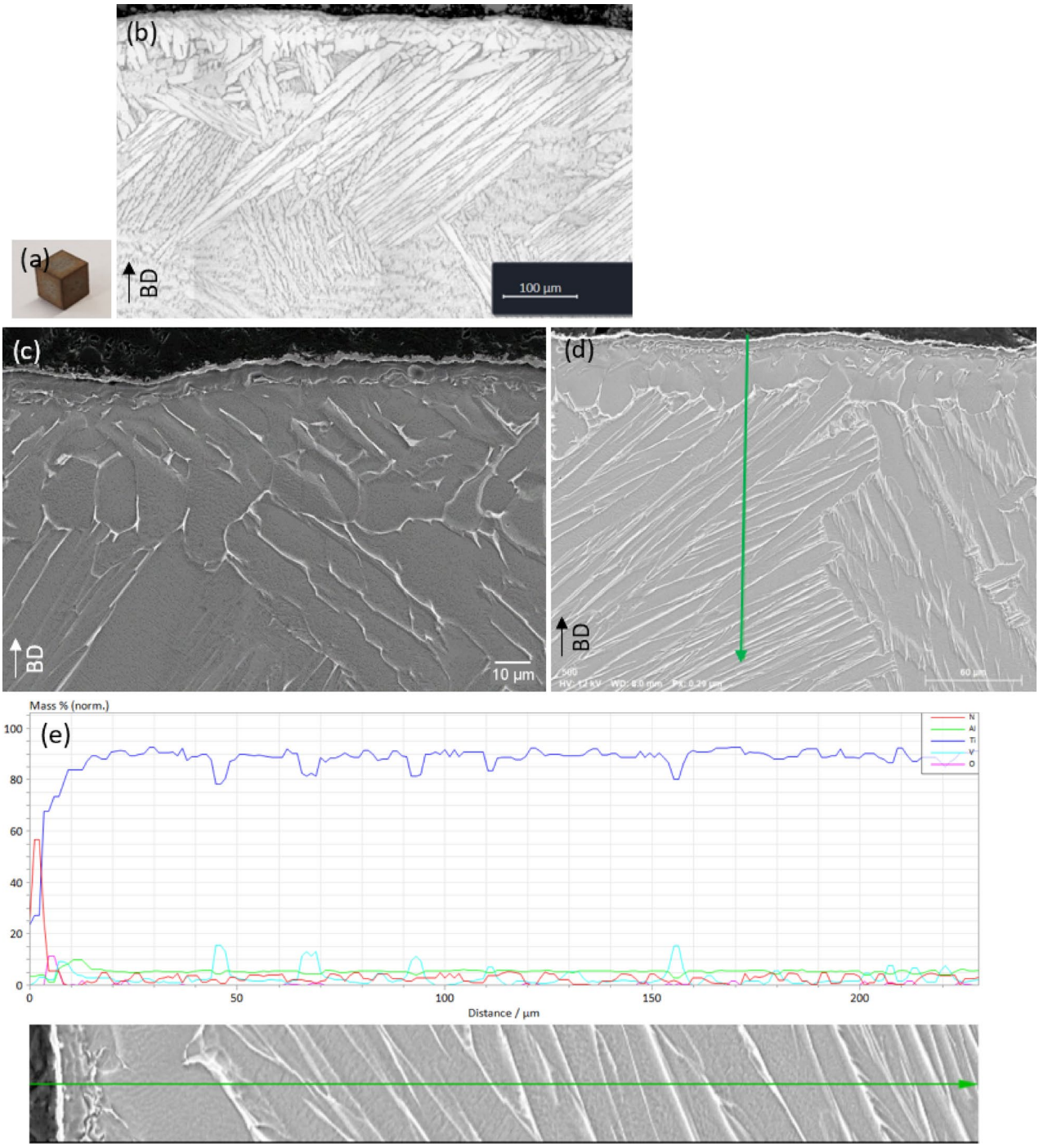

Fig. 28. Gas nitriding of S22 sample, at 1200 °C for 10 min in electric furnace. (**a**) sample S22 after nitriding, (**b**) OM of cross-section microstructure on top part of the sample, (**c**) SEM image on the top part of S22 cross-section, (**d**,**e**) line scan SEM–EDS analysis on the top of S22 cross-section.

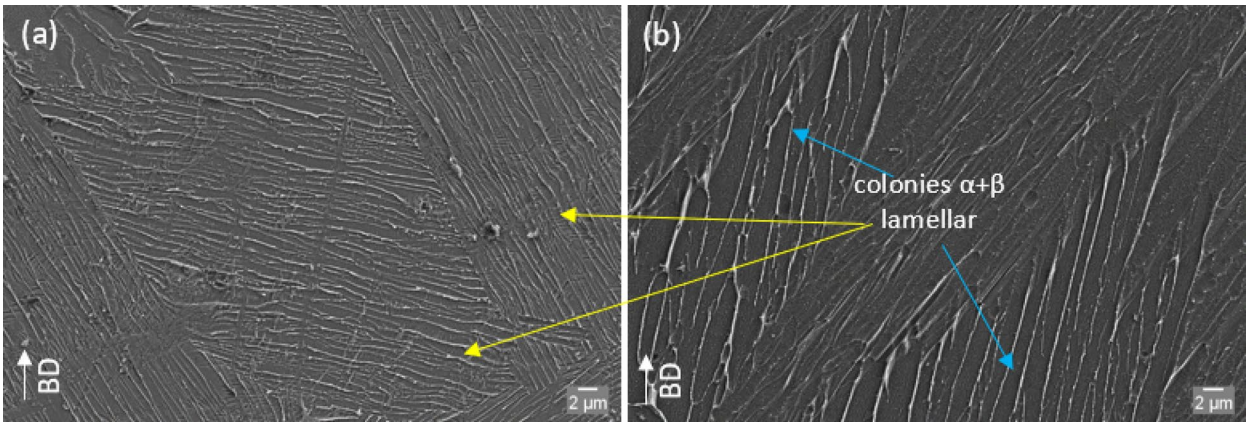

Fig. 29. Internal microstructure after nitriding at 1200 °C, 10 min. LOM and SEM micrographs after nitriding in SF (**a**) respectively EF (**b**).

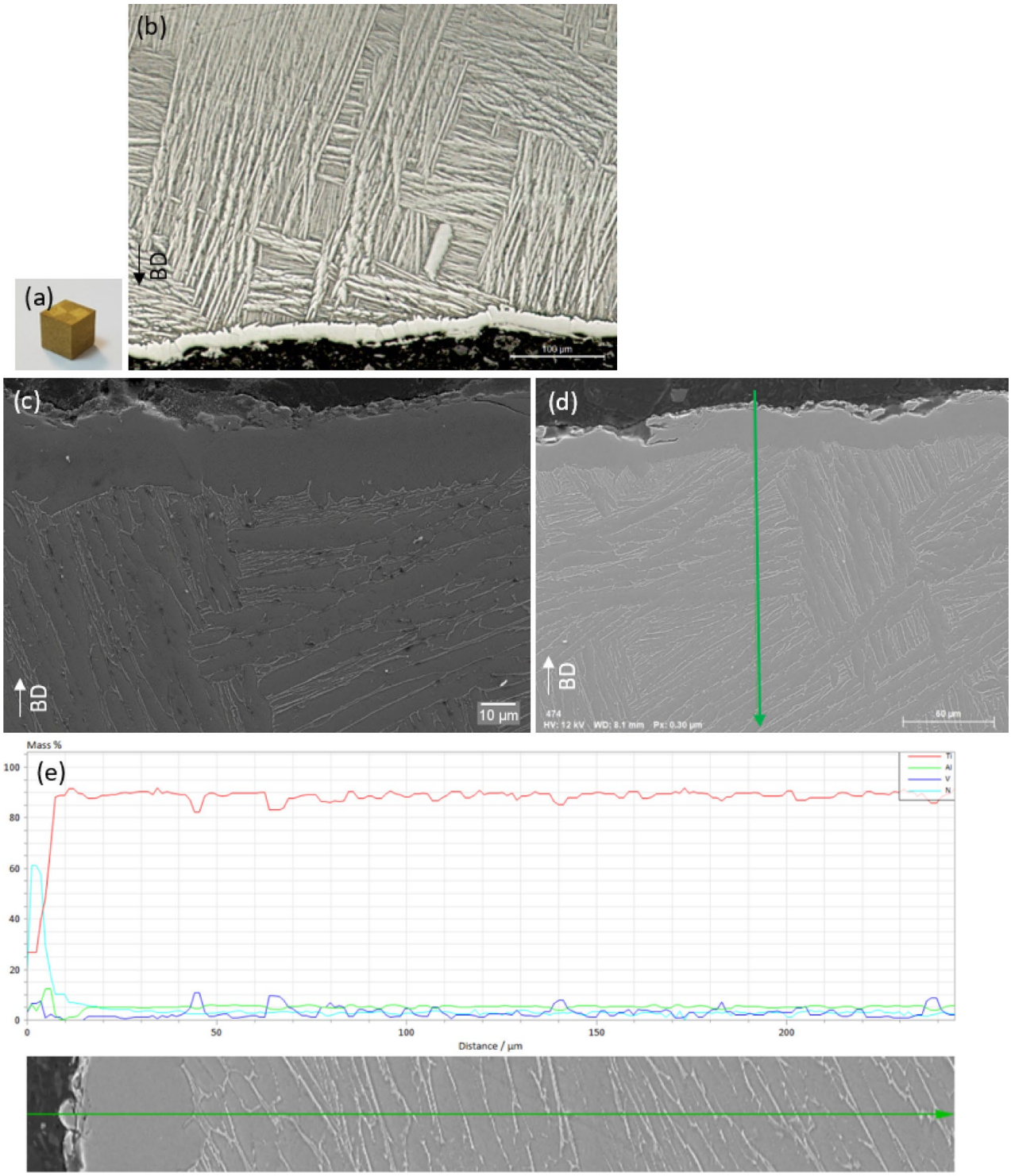

Fig. 30. Gas nitriding at 1200 °C for 15 min in solar furnace. (**a**) sample S15 after nitriding in SF, (**b**) cross-section microstructure from LOM on top part of the sample, (**c**) SEM image on the top part of S15 sample, (**d**,**e**) line scan SEM–EDS analysis on the top of S15 sample cross-section.

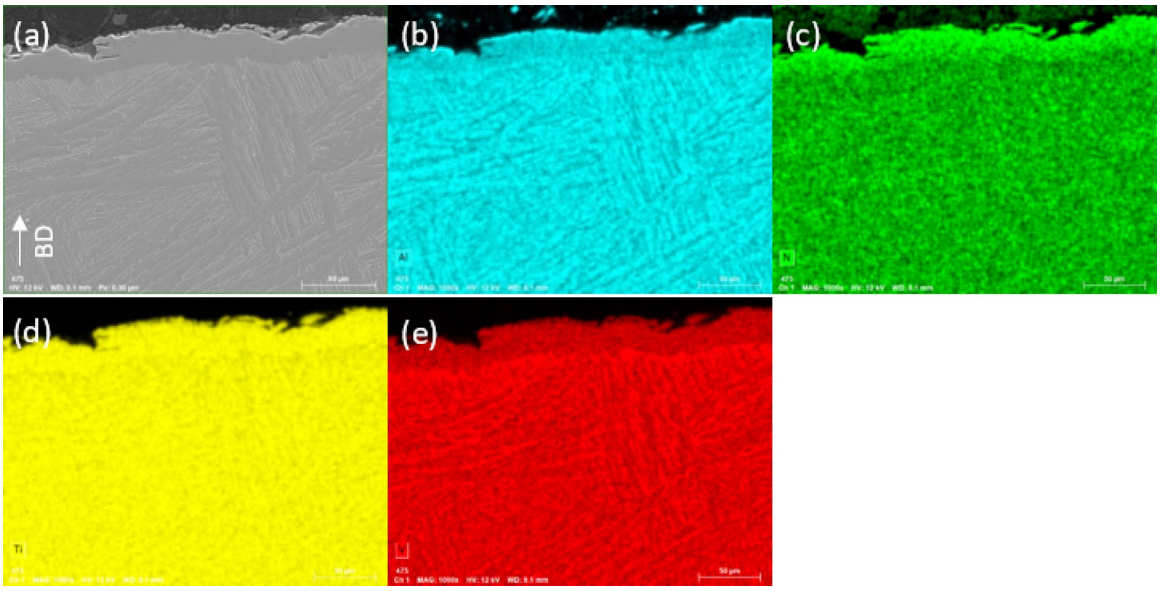

Fig. 31. SEM–EDS maps showing elemental distributions of chemical elements of S15 cross-section view after gas nitriding in SF at 1200 °C, 15 min. (**a**) area of interest, (**b**–**e**) distribution of Al, N, Ti, V.

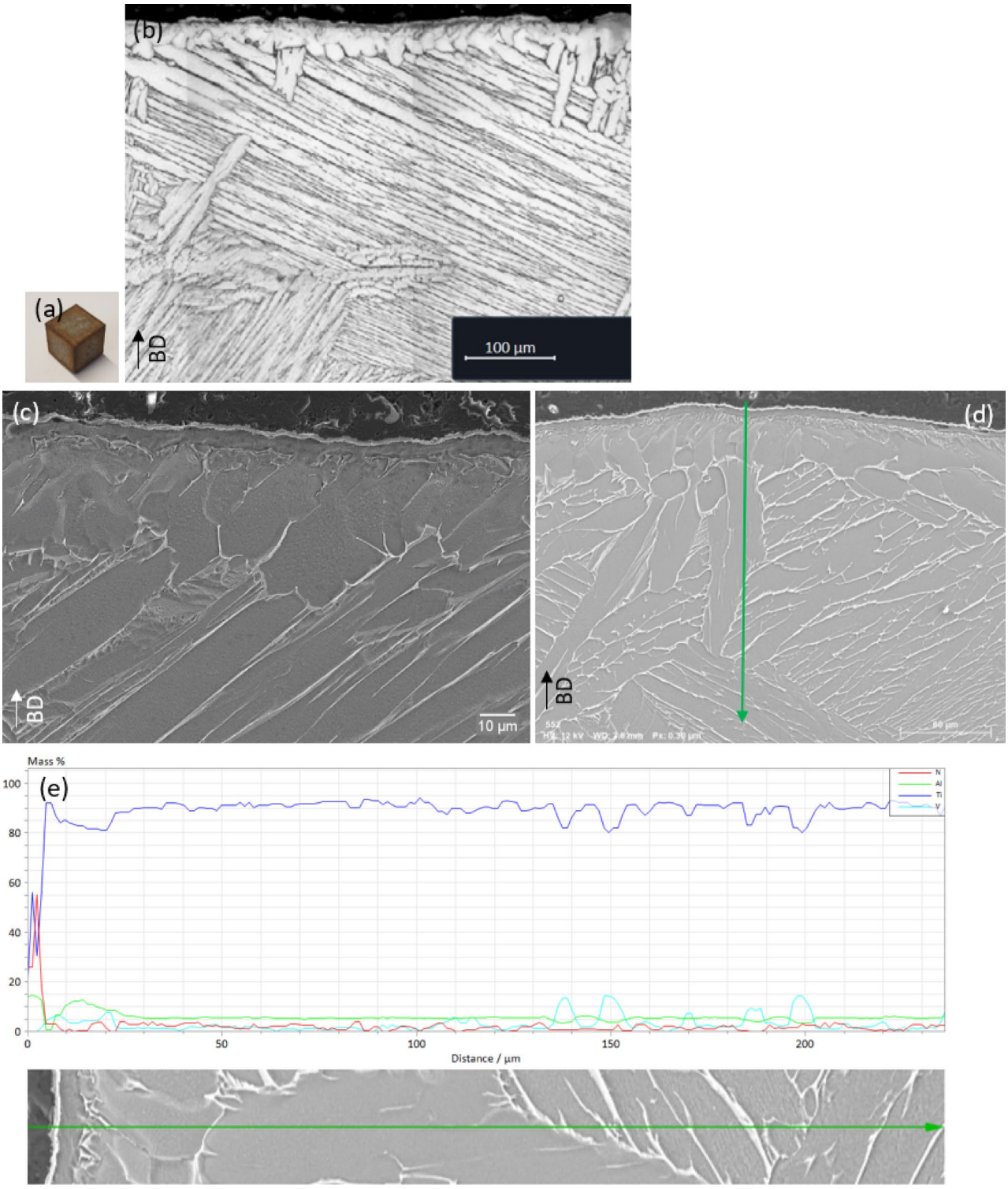

Fig. 32. Gas nitriding of S24 sample, at 1200 °C for 15 min in electric furnace. (**a**) sample S24 after nitriding, (**b**) OM of cross-section microstructure on top part of the sample, (**c**) SEM image on the top part of S22 cross-section, (**d**,**e**) line scan SEM–EDS analysis on the top of S24 cross-section.

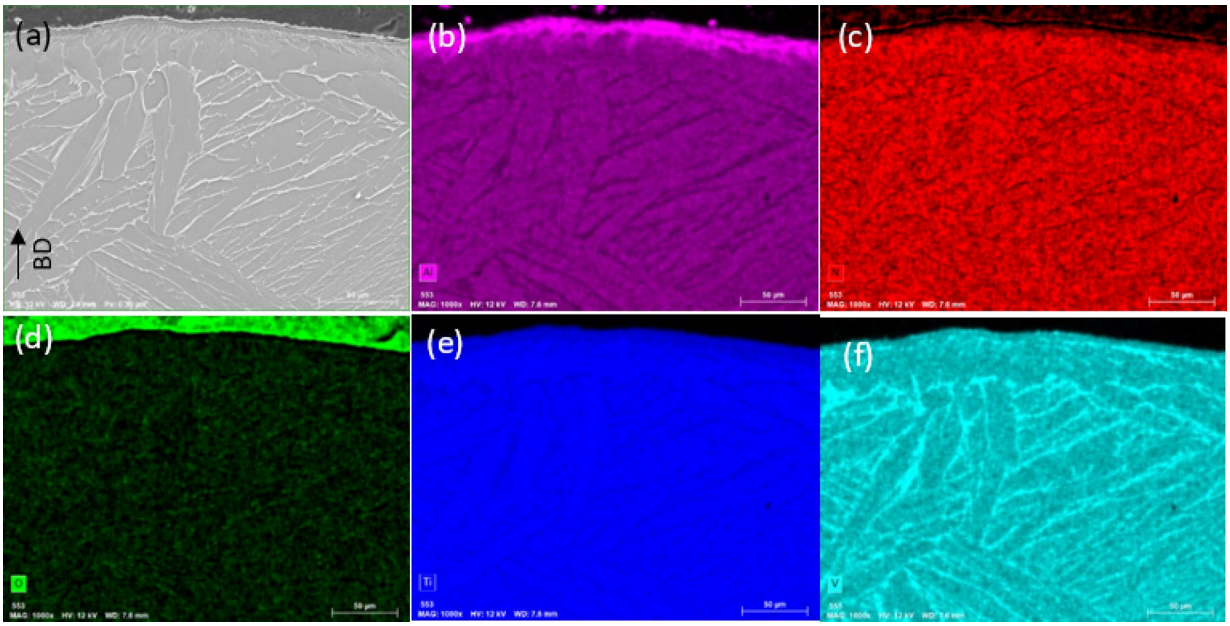

Fig. 33. SEM–EDS maps showing elemental distributions of chemical elements of S24 cross-section view after gas nitriding in EF at 1200 °C, for 15 min. (**a**) area of interest, (**b**–**f**) distribution of Al, N, O, Ti, V.

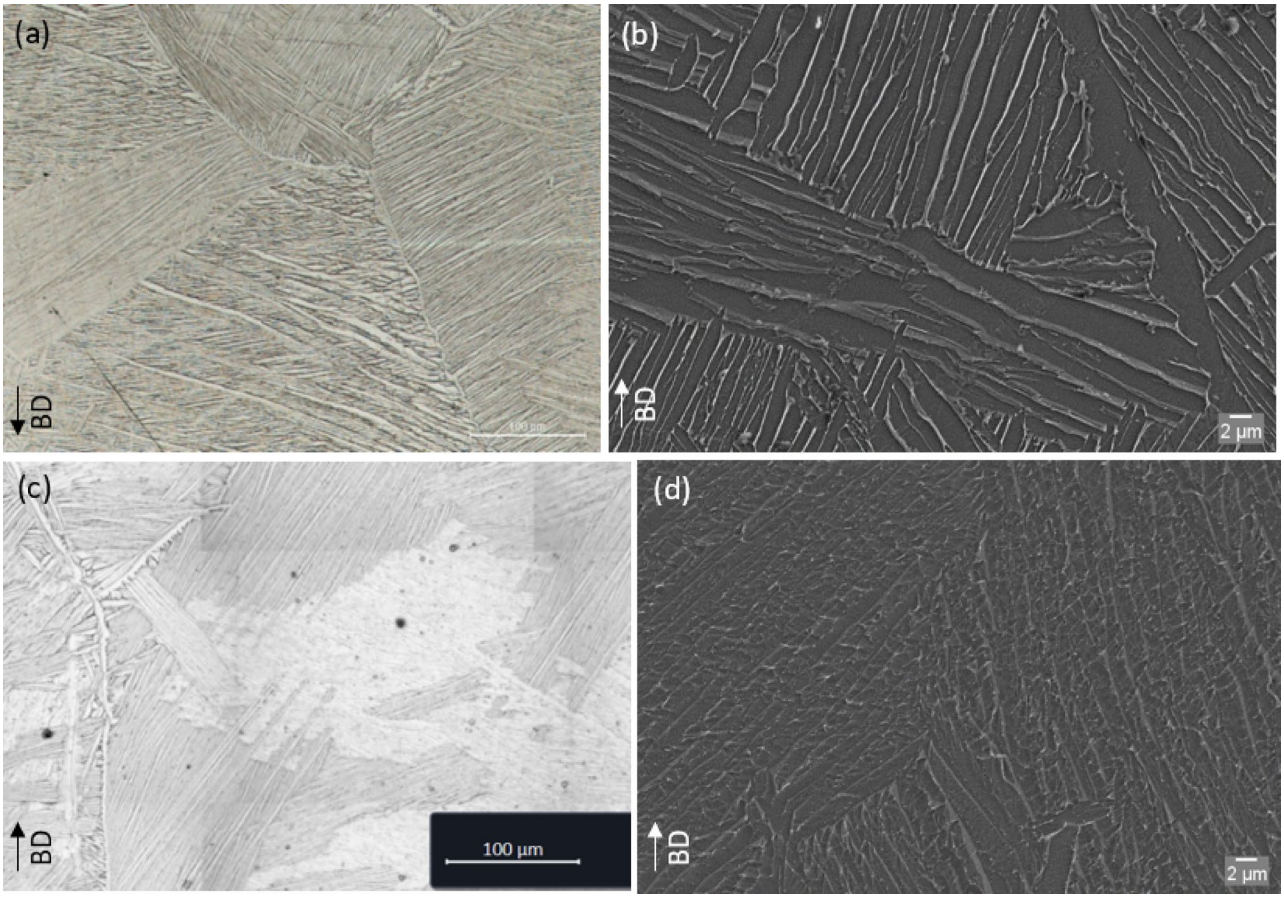

Fig. 34. Internal microstructure after nitriding at 1200 °C, 15 min. LOM and SEM micrographs after nitriding in SF (**a**,**b**) respectively EF (**c**,**d**).

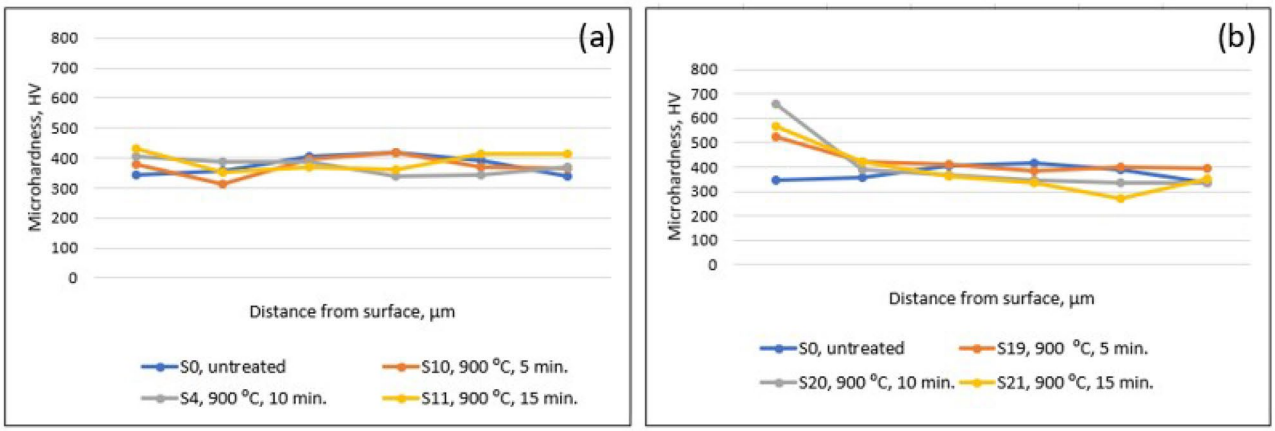

Fig. 35. Microhardness profile of samples nitrided at 900 °C. (**a**) solar furnace, (**b**) electric furnace.

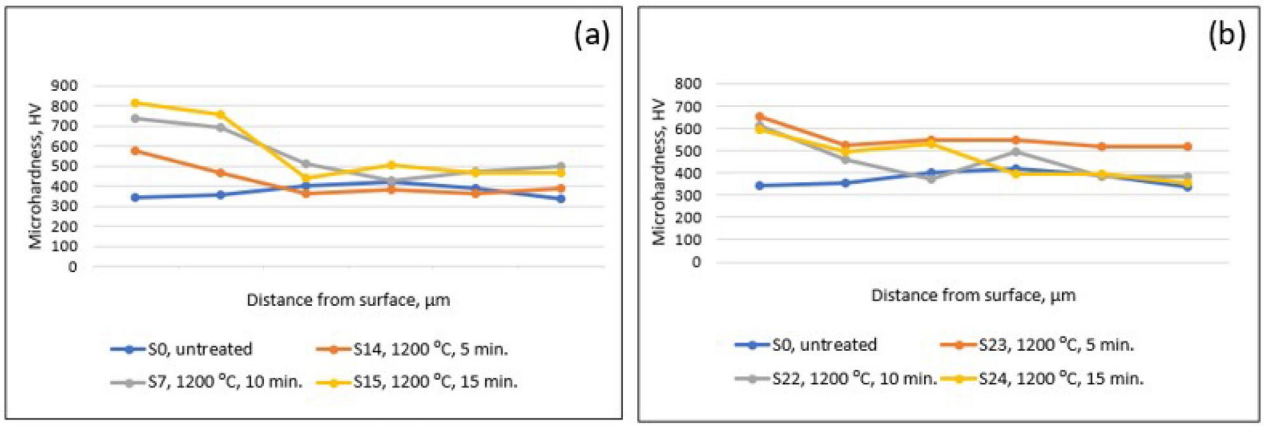

Fig. 36. Microhardness profile of samples gas nitrided at 1200 °C in solar furnace (**a**,**b**) electric furnace.

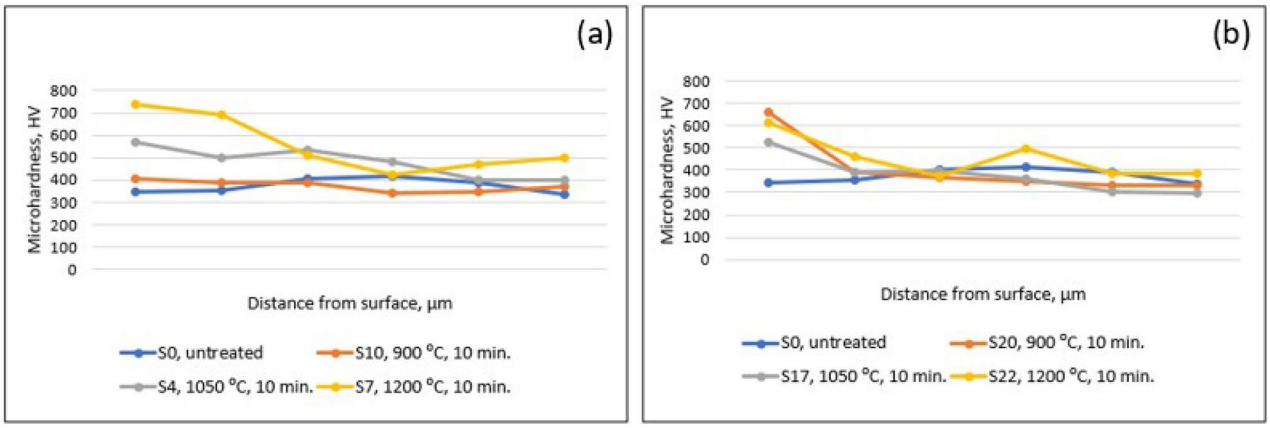

Fig. 37. Microhardness profile of samples of SLM Ti6Al4V nitrided for 10 min. at 900 °C, 1050 °C, and 1200 °C in solar furnace (**a**) and electric furnace (**b**).

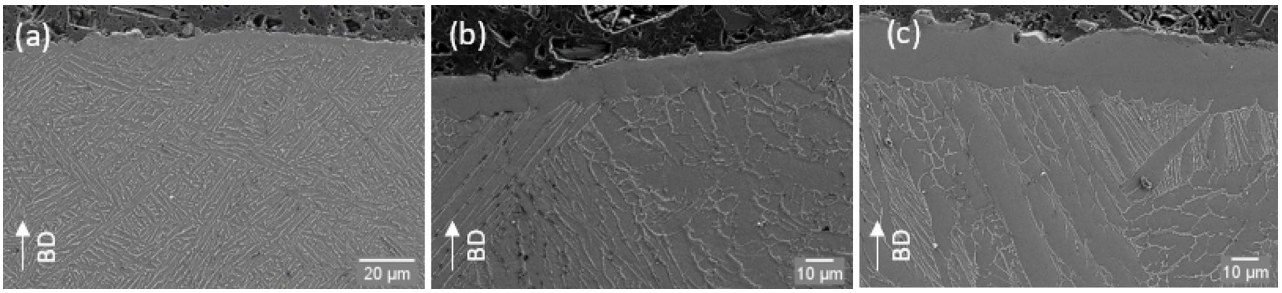

Fig. 38. Evolution of the nitrided layer after nitriding for 10 min at 900 °C (**a**), 1050 °C (**b**), and 1200 °C (**c**) in SF.

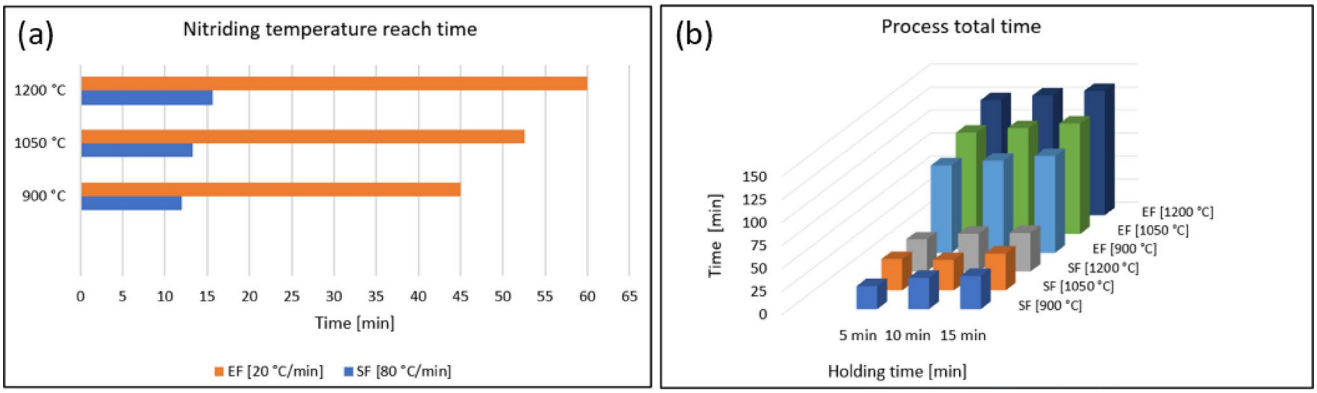

Fig. 39. Times related to gas nitriding thermochemical process in SF and EF. (**a**) Heating times in SF and EF; (**b**) Nitriding total times in SF and EF, respectively.

Data availability

All original data generated and/or analysed in the current study are included in the article, further inquiries can be directed to the corresponding author.

Received: 9 May 2025; Accepted: 24 July 2025
Published online: 02 August 2025

References

1. Kao, W. H., Su, Y. L., Horng, J. H. & Chang, C. Y. Tribological, electrochemical and biocompatibility properties of Ti6Al4V alloy produced by selective laser melting method and then processed using gas nitriding, CN or Ti-C:H coating treatments. *Surf. Coat. Tech.* **350**, 172–187. https://doi.org/10.1016/j.surfcoat.2018.07.011 (2018).
2. Valente, E. H., Jellesen, M. S., Somers, A. J. & Christiansen, T. L. Gaseous surface hardening of Ti–6Al–4V fabricated by selective laser melting. *Surf. Coat. Tech.* **383**, 125278. https://doi.org/10.1016/j.surfcoat.2019.125278 (2020).
3. Meier, B. et al. Toward a sustainable laser powder bed fusion of Ti6Al4V: Powder reuse and its effects on material properties during a single batch regime. *Sustain. Mater. Techno.* **36**, e00626. https://doi.org/10.1016/j.susmat.2023.e00626 (2023).
4. Kim, H. K. et al. Atmosphere gas carburizing for improved wear resistance of pure titanium fabricated by additive manufacturing. *Mater. Trans.* **58**, 592–595. https://doi.org/10.2320/matertrans.M2016361 (2017).
5. Lee, D. B., Pohrelyuk, I., Yaskiv, O. & Lee, J. C. Gas nitriding and subsequent oxidation of Ti–6Al–4V alloys. *Nanoscale Res. Lett.* **7**, 1–5. https://doi.org/10.1186/1556-276X-7-21 (2012).
6. Pohrelyuk, I. & Fedirko, V. Chemico-thermal treatment of titanium alloys—nitriding. In: *Titanium Alloys—Towards Achieving Enhanced Properties for Diversified Applications*. InTech, https://doi.org/10.5772/36546 (2012).
7. Lee, D. B. et al. Oxidation of nitride layers formed on Ti-6Al-4V alloys by gas nitriding. *Met Mater Int* **17**, 471–477. https://doi.org/10.1007/s12540-011-0627-9 (2011).
8. Zhecheva, A., Sha, W., Malinov, S. & Long, A. Enhancing the microstructure and properties of titanium alloys through nitriding and other surface engineering methods. *Surf. Coat. Technol.* **200**, 2192–2207. https://doi.org/10.1016/j.surfcoat.2004.07.115 (2005).
9. Zhao, X. et al. Combined effect of TiN coating and surface texture on corrosion-wear behavior of selective laser melted CP-titanium in simulated body fluid. *J. Alloys Compd.* **816**, 152667. https://doi.org/10.1016/j.jallcom.2019.152667 (2020).
10. Czerwinski, F. Thermochemical treatment of metals. *Heat Treat. Conv. Novel Appl.* **5**, 73–112. https://doi.org/10.5772/51566 (2012).
11. Guo, B. et al. Microstructure and tribological properties of in situ synthesized TiN/Ti3Al intermetallic matrix composite coatings on titanium by laser cladding and laser nitriding. *Mater. Sci. Eng., A* **480**, 404–410. https://doi.org/10.1016/j.msea.2007.07.010 (2008).
12. Nolan, D., Huang, S. W., Leskovsek, V. & Braun, S. Sliding wear of titanium nitride thin films deposited on Ti–6Al–4V alloy by PVD and plasma nitriding processes. *Surf. Coat. Technol.* **200**, 5698–5705. https://doi.org/10.1016/j.surfcoat.2005.08.110 (2006).

13. Leng, Y. X. et al. Fabrication of Ti–O/Ti–N duplex coatings on biomedical titanium alloys by metal plasma immersion ion implantation and reactive plasma nitriding/oxidation. *Surf. Coat. Technol.* **138**, 296–300. https://doi.org/10.1016/S0257-8972(00)01172-5 (2001).
14. Rodriguez, G. P., Herranz, G. & Romero, A. Solar gas nitriding of Ti6Al4V alloy. *Appl. Surf. Sci.* **283**, 445–452. https://doi.org/10.1016/j.apsusc.2013.06.128 (2013).
15. Rodríguez, G. P., Herranz, G., León, J. & Cañadas, I. Nitruración gaseosa de la aleación Ti6Al4V con energía solar concentrada. In X *Congreso Nacional de Materiales. Mondragon Unibertsitateko Zerbitzu, Spain* (2008).
16. Dwivedi, A., Khurana, M. K., Bala, Y. G. & Mishra, S. B. Microstructure and mechanical properties at elevated temperatures of as-built and heat-treated Inconel 718 produced through laser powder bed fusion processes. *Rapid Prototyp. J.* **3**, 635–650. https://doi.org/10.1108/RPJ-07-2024-0293 (2025).
17. Dwivedi, A., Khurana, M. K. & Bala, Y. G. Heat-treated nickel alloys produced using laser powder bed fusion-based additive manufacturing methods: A review. *Chin. J. Mech. Eng. Addit. Manuf. Front.* **2**, 100087. https://doi.org/10.1016/j.cjmeam.2023.100087 (2023).
18. Chicos, L. A. et al. Concentrated solar energy used for heat treatment of Ti6Al4V alloy manufactured by selective laser melting. *Sol. Energy* **173**, 76–88. https://doi.org/10.1016/j.solener.2018.07.069 (2018).
19. Dwivedi, A., Khurana, M. K. & Bala, Y. G. Effect of parameters on quality of IN718 parts using laser additive manufacturing. *Mater. Sci. Technol.* **40**, 633–648. https://doi.org/10.1177/02670836231219865 (2024).
20. Dwivedi, A., Khurana, M. K. & Bala, Y. G. A comparative study of porosity rate measurement methods and influence of energy density in Inconel 718 produced by laser powder bed fusion additive manufacturing process. *Int. J. Interact. Des. Manuf.* **19**, 2645–2658. https://doi.org/10.1007/s12008-024-01875-2 (2025).
21. Morton, P. A. et al. In situ selective laser gas nitriding for composite TiN/Ti–6Al–4V fabrication via laser powder bed fusion. *J. Mater. Sci. Technol.* **45**, 98–107. https://doi.org/10.1016/j.jmst.2019.11.009 (2020).
22. Liu, L. et al. In-situ nitrogen strengthening of selective laser melted Ti6Al4V with superior mechanical performance. *Addit. Manuf.* **46**, 102142. https://doi.org/10.1016/j.addma.2021.102142 (2021).
23. Wei, W., Wu, W., Fan, S. & Duan, X. In-situ laser additive manufacturing of Ti6Al4V matrix composites by gas–liquid reaction in dilute nitrogen gas atmospheres. *Mater. Des.* **202**, 109578. https://doi.org/10.1016/j.matdes.2021.109578 (2021).
24. Issariyapat, A., Visuttipitukul, P., Umeda, J. & Kondoh, K. Refined grain formation behavior and strengthening mechanism of α-titanium with nitrogen fabricated by selective laser melting. *Addit. Manuf.* **36**, 101537. https://doi.org/10.1016/j.addma.2020.101537 (2020).
25. Fernández-González, D. et al. Concentrated solar energy applications in materials science and metallurgy. *Sol. Energy* **170**, 520–540. https://doi.org/10.1016/j.solener.2018.05.065 (2018).
26. Fernández-González, D. A state-of-the-art review on materials production and processing using solar energy. *Miner. Process. Extr. Metall. Rev.* https://doi.org/10.1080/08827508.2023.2243008r (2023).
27. Olıas, J. S., Garcıa, I. & Vazquez, A. J. Synthesis of TiN with solar energy concentrated by a Fresnel lens. *Mater. Lett.* **38**, 379–385. https://doi.org/10.1016/S0167-577X(98)00193-1 (1999).
28. García, I., Sánchez-Olías, J., Damborenea, J. J. & Vázquez, A. J. Síntesis de nitruro de titanio mediante láser y energía solar concentrada. *Rev. Metal.* **34**, 109–113 (1998).
29. García, I., Sánchez-Olías, J., Damborenea, J. J. & Vázquez, A. J. A new method for materials synthesis: Solar energy concentrated by Fresnel lens, In *Journal of Physic IV France, Proceedings of the 9th Solar PACES International Symposium on Solar Thermal Concentrating Technologies, 9 (PR3)* 435–440, (1999).
30. Rodriguez, J., Cañadas, I. & Zarza, E. New PSA high concentration solar furnace SF40. In *AIP conference proceedings* 070028, (2016).
31. Schindelin, J. et al. Fiji: an open-source platform for biological-image analysis. *Nat. Methods* **9**, 676–682. https://doi.org/10.1038/nmeth.2019 (2012).
32. Thijs, L., Verhaeghe, F., Craeghs, T., Van Humbeeck, J. & Kruth, J. P. A study of the microstructural evolution during selective laser melting of Ti–6Al–4V. *Acta Mater.* **58**, 3303–3312. https://doi.org/10.1016/j.actamat.2010.02.004 (2010).
33. Vrancken, B., Thijs, L., Kruth, J. P. & Van Humbeeck, J. Heat treatment of Ti6Al4V produced by selective laser melting: Microstructure and mechanical properties. *J. Alloy. Compd.* **541**, 177–185. https://doi.org/10.1016/j.jallcom.2012.07.022 (2012).
34. Chicos, L. A. et al. Effect of concentrated solar energy on microstructure evolution of selective laser melted Ti-6Al-4V alloy. *Int J Adv Manuf Technol* **118**, 3183–3207. https://doi.org/10.1007/s00170-021-08136-6 (2021).
35. Liu, L. Surface hardening of titanium alloys by gas phase nitridation under kinetic control, PhD thesis, Case Western Reserve University, January, 2005, https://etd.ohiolink.edu/acprod/odb_etd/ws/send_file/send?accession=case1094223428&disposition=inline (2005).
36. Malinov, S., Zhecheva, A. & Sha, W. Relation between the microstructure and properties of commercial titanium alloys and the parameters of gas nitriding. *Met. Sci. Heat Treat.* **46**, 286–293 (2004).
37. Frantsevich, I. N., Grishnova, L. A. & Tikush, V. L. Reaction of titanium with nitrogen during heating by radiant energy. *Soviet Powder Metallurgy and Metal Ceramics* **25**, 375–377. https://doi.org/10.1007/BF00813948 (1986).
38. Osterman, V. Gas Nitriding of Titanium, https://solaratm.com/tech-downloads/gas-nitriding-of-titanium/, Accessed 15 September 2024.
39. Xiu, M., Tan, Y. T., Raghavan, S., Goh, M. H. & Nai, M. L. The effect of heat treatment on microstructure, microhardness, and pitting corrosion of Ti6Al4V produced by electron beam melting additive manufacturing process. *Int. J. Adv. Manuf. Technol.* **120**, 1281–1293. https://doi.org/10.1007/s00170-022-08839-4 (2022).
40. Cao, S. et al. Static coarsening behaviour of lamellar microstructure in selective laser melted Ti–6Al–4V. *J Mater. Sci. Technol.* **35**, 1578–1586. https://doi.org/10.1016/j.jmst.2019.04.008 (2019).
41. Zhang, D. Effect of heat treatment on the tensile behavior of selective laser melted Ti–6Al–4V by in situ X-ray characterization. *Acta. Mater.* **189**, 93–104. https://doi.org/10.1016/j.actamat.2020.03.003 (2020).
42. Takesue, S., Kikuchi, S., Akebono, H., Morita, T. & Komotori, J. Characterization of surface layer formed by gas blow induction heating nitriding at different temperatures and its effect on the fatigue properties of titanium alloy. *Results Mater.* **5**, 100071. https://doi.org/10.1016/j.rinma.2020.100071 (2020).
43. Takesue, S., Kikuchi, S., Misaka, Y., Morita, T. & Komotori, J. Rapid nitriding mechanism of titanium alloy by gas blow induction heating. *Surf. Coat. Technol.* **399**, 126160. https://doi.org/10.1016/j.surfcoat.2020.126160 (2020).
44. Ahmed, F. S. *et al*. Influence of α-phase morphology on mechanical characteristics, cycle oxidation, and hot corrosion behavior of Ti–6Al–3Mo–2Nb–2Zr–2Sn–1.5Cr alloy. *Metallogr. Microstruct. Anal.* **11,** 746–760. https://doi.org/10.1007/s13632-022-00884-5 (2022).
45. Dong, E., Yu, W., Cai, Q., Cheng, L. & Shi, J. High-temperature oxidation kinetics and behavior of Ti–6Al–4V alloy. *Oxid Met* **88**, 719–732. https://doi.org/10.1007/s11085-017-9770-0 (2017).
46. Wang, S., Liang, Y., Sun, H., Feng, X. & Huang, C. Oxygen induced phase transformation in TC21 alloy with a lamellar microstructure. *Metals* **11**, 163. https://doi.org/10.3390/met11010163 (2021).
47. Lee, D. B. et al. Gas Nitriding and oxidation of Ti-6Al-4V alloy. *Defect Diffus. Forum* **382**, 155–159. https://doi.org/10.4028/www.scientific.net/DDF.382.155 (2018).
48. Vilaro, T., Colin, C. & Bartout, J. D. As-fabricated and heat-treated microstructures of the Ti-6Al-4V alloy processed by selective laser melting. *Metall. and Mater. Trans. A.* **42**, 3190–3199. https://doi.org/10.1007/s11661-011-0731-y (2011).

49. Lütjering, G., Williams, J. C. & Gysler, A. Microstructure and mechanical properties of titanium alloys. *Microstruct. Prop. Mater.* 1–77. https://doi.org/10.1142/9789812793959_0001 (2000).
50. Sercombe, T., Jones, N., Day, R. & Kop, A. Heat treatment of Ti-6Al-7Nb components produced by selective laser melting. *Rapid. Prototyp. J.* **14**, 300–400. https://doi.org/10.1108/13552540810907974 (2008).
51. Lutjering, G. Influence of processing on microstructure and mechanical properties of (α+β) titanium alloys. *Mater. Sci. Eng. A* **243**, 32–45. https://doi.org/10.1016/S0921-5093(97)00778-8 (1998).
52. Collins, C. R., Dear, F. F., Rugg, D. & Dye, D. The effect of dissolved nitrogen on the fatigue behavior of Ti-6Al-4V. *Metall. Mater. Trans. A* **52**, 1596–1608. https://doi.org/10.1007/s11661-021-06147-2 (2021).
53. Cuthill, J. R., Hayes, W. D. & Seebold, R. E. Nitriding phenomena in titanium and the 6Al-4V titanium alloy. *J. Res. Natl. Bur. Stand Phys. Chem.* **64**, 119–125. https://doi.org/10.6028/jres.064A.010 (1960).
54. Rahman, M. et al. Structural and tribological properties of the plasma nitrided Ti-alloy biomaterials: Influence of the treatment temperature. *Surf. Coat. Technol.* **201**, 4865–4872. https://doi.org/10.1016/j.surfcoat.2006.07.178 (2007).
55. Almeida, G. F. et al. Effect of plasma nitriding on the creep and tensile properties of the Ti–6Al–4V alloy. *Metals* **8**, 618. https://doi.org/10.3390/met8080618 (2018).
56. Luk'yanenko, A. G. *et al.* Gas nitriding of the near-beta-titanium alloy. archives of metallurgy and *Materials* **68,** 431–438. https://doi.org/10.24425/amm.2023.142419 (2023).
57. Oliveira, F. A. et al. Reactions of IVa- group metals, Ti and Zr, with uncracked NH_3 gas at a temperature in the range between 600 and 800 °C under heating with concentrated solar beam at PSA. *Sol. Energy* **138**, 119–127. https://doi.org/10.1016/j.solener.2016.09.012 (2016).
58. Zhang, S. Z., Zhou, B., Liu, N. & Chen, L. Q. Effects of microstructure and rare-earth constituent on the oxidation behavior of Ti–5.6 Al–4.8 Sn–2Zr–1Mo–0.35 Si–0.7 Nd titanium alloy. *Oxid. Met.* **81**, 373–382. https://doi.org/10.1007/s11085-013-9445-4 (2014).
59. Diamanti, M. V., Codeluppi, S., Cordioli, A. & Pedeferri, M. P. Effect of thermal oxidation on titanium oxides' characteristics. *J. Exp. Nanosci.* **4**, 365–372. https://doi.org/10.1080/17458080902769937 (2009).
60. Haque, F. Z., Nandanwar, R. & Singh, P. Evaluating photodegradation properties of anatase and rutile TiO_2 nanoparticles for organic compounds. *Opti* **128**, 191–200. https://doi.org/10.1016/j.ijleo.2016.10.025 (2017).
61. Wang, B. *et al.* Low temperature oxidation of titanium nitride under high oxygen pressure by O_2-HIP. In *Journal of Materials. Proceedings of the International Conference on Hot Isostatic Pressing Kobe, Japan*. https://doi.org/10.2240/azojomo0308 (2011).
62. Bakri, A. S. *et al.* Effect of annealing temperature of titanium dioxide thin films on structural and electrical properties, In *AIP Conf Proc*, AIP Publishing. https://doi.org/10.1063/1.4968283 (2017).
63. Kim, D. J., Hahn, S. H., Oh, S. H. & Kim, E. J. Influence of calcination temperature on structural and optical properties of TiO_2 thin films prepared by sol–gel dip coating. *Mater. Lett.* **57**, 355–360. https://doi.org/10.1016/S0167-577X(02)00790-5 (2002).
64. Partowafkan, S., Pour-Ali, S., Tavangar, R. & Hejazi, S. Thermal oxidation of Ti-6Al-4V ELI with an ultrafine-grained surface at 500 °C: Oxidation kinetics, oxide characterization and corrosion performance. *Surf. Coat. Technol.* **469**, 129794. https://doi.org/10.1016/j.surfcoat.2023.129794 (2023).
65. Carp, O., Huisman, C. L. & Reller, A. Photoinduced reactivity of titanium dioxide. *Prog. Solid State Chem.* **32**, 33–177. https://doi.org/10.1016/j.progsolidstchem.2004.08.001 (2004).
66. Zhang, H. & Banfield, J. F. Thermodynamic analysis of phase stability of nanocrystalline titania. *J. Mater. Chem.* **8**, 2073–2076. https://doi.org/10.1039/A802619J (1998).
67. Zhang, Q. & Li, C. High temperature stable anatase phase titanium dioxide films synthesized by mist chemical vapor deposition. *Nanomaterials* **10**, 911. https://doi.org/10.3390/nano10050911 (2020).
68. Hanaor, D. A. & Sorrell, C. C. Review of the anatase to rutile phase transformation. *J. Mater. Sci.* **46**, 855–874. https://doi.org/10.1007/s10853-010-5113-0 (2011).
69. Luttrell, T. et al. Why is anatase a better photocatalyst than rutile? -Model studies on epitaxial TiO_2 films. *Sci. Rep.* **4**, 4043. https://doi.org/10.1038/srep04043 (2014).
70. Lütjering, G. & Williams, J. C. *Titanium Book* (Springer, 2007).
71. Yang, Y. et al. Microstructure and fatigue performance of Ti6Al4V produced by laser powder bed fusion after post-heat treatment. *Appl. Sci.* **13**, 1828. https://doi.org/10.3390/app13031828 (2023).
72. Kumar, P. & Ramamurty, U. Microstructural optimization through heat treatment for enhancing the fracture toughness and fatigue crack growth resistance of selective laser melted Ti6Al4V alloy. *Acta Mater.* **169**, 45–59. https://doi.org/10.1016/j.actamat.2019.03.003 (2019).
73. Ponticaud, C., Guillou, A. & Lefort, P. Direct gaseous nitridation of the Ti–6Al–4V alloy by nitrogen. *Phys. Chem. Chem. Phys.* **2**, 1709–1715. https://doi.org/10.1039/A909520I (2000).
74. Pérez, P. Influence of nitriding on the oxidation behaviour of titanium alloys at 700 C. *Surf. Coat. Technol.* **191**, 293–302. https://doi.org/10.1016/j.surfcoat.2004.04.066 (2005).
75. Liu, G. et al. First-principles analysis on the nitrogen adsorption and diffusion in Ti alloy towards clarified diffusion mechanism in nitriding. *J. Market. Res.* **21**, 1479–1489. https://doi.org/10.1016/j.jmrt.2022.09.112 (2022).
76. Leyens, C. & Peters, M. *Titanium and Titanium Alloys: Fundamentals and Applications* (John Wiley & Sons, 2003).
77. Carrozza, A. et al. Effect of aging and cooling path on the super β-transus heat-treated Ti-6Al-4V alloy produced via Electron Beam Melting (EBM). *Materials* **15**, 4067. https://doi.org/10.3390/ma15124067 (2022).
78. Kazantseva, N. *et al.* Comparative analysis of the structure and properties of titanium and cobalt medical alloys manufacturing by 3D printing. In *Conference of the Rapid Product Development Association of South Africa (RAPDASA) 20th Annual International Conference, Emoya Estate, Bloemfontein* (2019).
79. Huang, Q. et al. Specific heat treatment of selective laser melted Ti–6Al–4V for biomedical applications. *Front. Mater. Sci.* **9**, 373–381. https://doi.org/10.1007/s11706-015-0315-7 (2015).

Acknowledgements

We thank the Plataforma Solar de Almeria – CIEMAT for providing access to its installations, the support of its scientific and technical staff, and the financial support of the SFERA-III project (Grant Agreement No 823802). This project has received funding from the European Union's Horizon 2020 research and innovation programme under grant agreement No 823717-ESTEEM3. We also acknowledge to structural founds project PRO-DD (POS-CCE, O.2.2.1, ID 123, SMIS 2637, ctr. No 11/2009) for partly providing the infrastructure used in this work.

Author contributions

L.-A. Chicos: Conceptualization, Writing-original draft, Writing-review and editing, Funding acquisition, Project administration, Investigation, Data curation; J. Rodríguez: Investigation, Supervision, Methodology, Resources; I. Cañadas: Investigation, Supervision, Resources; J. Galindo: Investigation, Supervision, Resources; G. Cempura: Investigation, Supervision, Methodology, Resources; A. Kruk: Supervision, Visualization, Meth-

odology, Resources; M. Ziętara: Investigation, Supervision; A. Gruszczyński: Investigation, Resources; S. M. Zaharia: Supervision, Writing-review and editing; M. A. Pop: Investigation, Resources; C. Lancea: Software, Visualization.

Declarations

Competing interests

The authors declare no competing interests.

Additional information

Correspondence and requests for materials should be addressed to L.-A.C.

Reprints and permissions information is available at www.nature.com/reprints.

Publisher's note Springer Nature remains neutral with regard to jurisdictional claims in published maps and institutional affiliations.